

## ABSTRACT

### Algorithms for Fast Power Amplifier Load Impedance and Input Power Optimization Using the Power Smith Tube

Joseph Barkate, M.S.E.C.E

Mentor: Charles P. Baylis II, Ph.D.

The increasing number of devices occupying the finite wireless broadband spectrum has led to serious concerns regarding spectral congestion. To facilitate radar and communication spectral coexistence, reconfigurable, adaptive amplifiers are expected to be a critical component in future cognitive radar transmitters. This work details a method to visualize and simultaneously optimize the load reflection coefficient and input power of a power amplifier device in order to achieve the highest possible efficiency while meeting a predefined spectral spreading constraint. The proposed vector-based search utilizes gradients as well as momentum in the Power Smith Tube in order to optimize accurately with as few experimental queries as possible. This method is proven to be feasible in higher dimensions, allowing for future implementation in real-time reconfigurable power amplifiers.

Algorithms for Fast Power Amplifier Load Impedance and Input Power Optimization Using the  
Power Smith Tube

by

Joseph Barkate, B.S.E.C.E.

A Thesis

Approved by the Department of Electrical and Computer Engineering

---

Kwang Y. Lee, Ph.D., Chairperson

Submitted to the Graduate Faculty of  
Baylor University in Partial Fulfillment of the  
Requirements for the Degree  
of  
Master of Science in Electrical and Computer Engineering

Approved by the Thesis Committee

---

Charles P. Baylis, Ph.D., Chairperson

---

Robert J. Marks II, Ph.D.

---

Byron Newberry, Ph.D.

Accepted by the Graduate School  
May 2016

---

J. Larry Lyon, Ph.D., Dean

Copyright © 2016 by Joseph Barkate

All rights reserved

## TABLE OF CONTENTS

LIST OF FIGURES	v
LIST OF TABLES	vii
ACKNOWLEDGMENTS	viii
CHAPTER ONE: INTRODUCTION	1
CHAPTER TWO: THE POWER SMITH TUBE	3
2.1 Motivation for 3D Search Space	3
2.1.1 Power Amplifier Background	3
2.1.2 Previous Design Approach	6
2.1.3 Prior Art	9
2.2 The Power Smith Tube	10
2.3 Power Smith Tube Measurement Results	18
2.4 Summary	23
CHAPTER THREE: FAST OPTIMIZATION IN THE POWER SMITH TUBE	24
3.1 Motivation for a Search Algorithm	24
3.2 Gradient-Based Search	28
3.2.1 Simulation Results	33
3.2.2 Measurement Results	38
3.3 Momentum Aided Search	44
3.4 Summary	52
CHAPTER FOUR: OPTIMIZATION IN HIGHER DIMENSIONS	54
4.1 Motivation for Higher Dimensional Optimization	55
4.2 Visualization in Higher Dimensions	56
4.2.1 Four-Dimensional Visualization	56
4.2.2 Five-Dimensional Visualization	62
4.3 Gradient Based Optimization in 4D	67
4.3.1 Search Background	67
4.3.2 Four-Dimensional Simulation Results	70
4.3.3 Five-Dimensional Simulation Results	73
4.4 Summary	76
CHAPTER FIVE: CONCLUSIONS	78
BIBLIOGRAPHY	80

## LIST OF FIGURES

Figure 2.1 Demonstration of linearity and efficiency tradeoffs.....	5
Figure 2.2 Measurement load-pull example .....	7
Figure 2.3 Measurement power sweep example.....	8
Figure 2.4 Power Smith Tube conceptualization .....	11
Figure 2.5 Simulated input power versus efficiency .....	13
Figure 2.6 Simulated ACPR and PAE contours .....	14
Figure 2.7 Preliminary Power Smith Tube design.....	15
Figure 2.8 Power Smith Tube visualization.....	16
Figure 2.9 Power Smith Tube visualization of Modelithics model .....	17
Figure 2.10 Lab measurement setup .....	19
Figure 2.11 Measured ACPR and PAE contours.....	20
Figure 2.12 Power Smith Tube visualization in measurement .....	22
Figure 2.13 Power Smith Tube visualization in measurement example two.....	22
Figure 3.1 Gradient evaluation example.....	30
Figure 3.2 Search vector logic example.....	31
Figure 3.3 Simulated Power Tube search trajectory for trial I .....	35
Figure 3.4 Simulated Power Tube search trajectory for trial II .....	36
Figure 3.5 Simulated Power Tube search trajectory for trial III.....	37
Figure 3.6 Simulated Power Tube search trajectory for trial IV.....	38
Figure 3.7 Simulated Power Tube search trajectory for trial V .....	38

Figure 3.8 Measured Power Tube search trajectory for trial I.....	41
Figure 3.9 Measured Power Tube search trajectory for trial II.....	41
Figure 3.10 Measured Power Tube search trajectory for trial III.....	42
Figure 3.11 Measured Power Tube search trajectory for trial IV.....	42
Figure 3.11 Measured Power Tube search trajectory for trial V.....	42
Figure 3.13 Momentum $\alpha = 0$ search trajectory for trial I.....	46
Figure 3.14 Momentum $\alpha = 0.2$ search trajectory for trial I.....	46
Figure 3.15 Momentum $\alpha = 0.4$ search trajectory for trial I.....	47
Figure 3.16 Momentum $\alpha = 0$ search trajectory for trial II.....	48
Figure 3.17 Momentum $\alpha = 0.2$ search trajectory for trial II.....	49
Figure 3.18 Momentum $\alpha = 0.4$ search trajectory for trial II.....	49
Figure 4.1 IV curves for Modelithics ADS model.....	57
Figure 4.2 Four-dimensional $V_{DS}$ ACPR diagram.....	58
Figure 4.3 Four-dimensional $V_{DS}$ ACPR and PAE diagram.....	60
Figure 4.4 Four-dimensional $V_{GS}$ ACPR diagram.....	61
Figure 4.5 Four-dimensional $V_{GS}$ ACPR and PAE diagram.....	62
Figure 4.6 Five-dimensional $V_{DS}$ and $V_{GS}$ ACPR diagram.....	64
Figure 4.7 Five-dimensional $V_{DS}$ and $V_{GS}$ ACPR and PAE diagram.....	66
Figure 4.8 Four-dimensional search trajectory for trial I.....	71
Figure 4.9 Four-dimensional search trajectory for trial II.....	72
Figure 4.10 Four-dimensional search trajectory for trial III.....	72
Figure 4.11 Five-dimensional search trajectory for trial I.....	74
Figure 4.12 Five-dimensional search trajectory for trial II.....	76

## LIST OF TABLES

Table 3.1 Summary of Power Tube simulation results.....	39
Table 3.2 Summary of Power Tube measurement results .....	43
Table 3.3 Summary of momentum-aided search results.....	52
Table 5.1 Summary of four-dimensional simulation results.....	73
Table 5.2 Summary of five-dimensional simulation results .....	75

## ACKNOWLEDGMENTS

I would like to acknowledge with my deepest gratitude my advisor Dr. Charles Baylis without whom this work would not have been possible. Under his guidance I have grown both professionally and personally through his unwavering support and genuine encouragement. Thanks also to Dr. Marks for lending his unique perspective, immense technical knowledge, and refreshing disposition, and Larry Cohen from the Naval Research Laboratory for contributing insights from his industry experiences and familiarity with practical applications. I would also like to thank Matthew Fellows for his expertise and previous work which provided the basis and tools needed for my research, as well as my Masters colleague Dylan Eustice, and the many team members of the WMCS lab. Special thanks to Keysight Technologies for their cost-free loan of Advanced Design System Software and Modelithics for providing measurement simulation models. I would also like to recognize the National Science Foundation for funding this work under grant ECCS-1343316.

Finally, I would like to thank my family members Ilona, Joe, and Vikki Barkate for their steadfast support, as well as Courtney Traber for her assistance and patience throughout the revision process.

## CHAPTER ONE

### Introduction

Demand for wireless broadband communications has risen to unprecedented heights due to recent technological advances. As a result, available spectrum is now a precious commodity. As the spectrum moves toward becoming overcrowded, wireless transmitting amplifiers must operate under increasingly stringent conditions. Spectral free space has become so valuable that in 2008 the FCC auctioned 700 MHz of spectrum for over 19 billion U.S. dollars. More recently, the National Broadband Plan of 2010 proposed the reallocation of 500MHz of spectrum for wireless broadband over a period of ten years. Much of this spectrum is either being taken from radar, or is requiring spectrum sharing between communication and radar systems. Despite the significant loss of operating spectrum, radar systems are still required to perform effectively. To allow radar transmitters to operate in this evolving paradigm, a new approach is needed.

One proposed solution for this dilemma is dynamic spectrum allocation, in which spectrum is allocated in real-time. Adaptive radar transmission facilitates dynamic spectrum allocation by adjusting operating characteristics in real-time in order to meet spectral requirements. The burden of reconfigurability falls heavily on power amplifiers, as their operating characteristics are directly correlated with signal quality [3,32,45]. This thesis presents a novel solution to the dynamic optimization of power amplifier circuitry through both visualization and direct optimization methods. The proposed optimization algorithms are designed to quickly reconfigure a power amplifier's load reflection

coefficient as well as input power based on the spectral environment. Not only would the performance of cognitive radar improve from direct optimization, but communication applications can utilize these techniques to increase proficiency. In addition, the fast, multi-parameter circuit optimizations can be applied to improve simulation- and measurement-based amplifier design through implementation in computer-aided design and measurement software.

The Power Smith Tube, which allows for visualization of both linearity and efficiency variations with load reflection coefficient and input power, is presented in Chapter Two. In Chapter Three, a gradient-based search is demonstrated that allows for fast optimization of the circuit parameters based on this visualization tool. Chapter Four then presents the idea of moving into search spaces of greater than three dimensions, where visualization and optimization approaches for four- and five-dimensional searches are presented. Finally, Chapter Five provides some conclusions based on the results and proposes future directions for this work.

## CHAPTER TWO

### The Power Smith Tube

The linear and efficient operation of power amplifiers is based on several design characteristics. Two design characteristics that have significant influence are the input power and the load reflection coefficient. Currently, in order to view the effect these characteristics have on power amplifier performance, designers typically examine each input parameter individually while holding the other constant. A new method to visualize the effects of varying the load impedance and the input power simultaneously would provide significant design and reconfiguration insight. This three-dimensional graph would allow concurrent visualization of multiple design criteria such as amplifier linearity and efficiency. The Power Smith Tube proposed in this chapter is a novel tool that achieves visualization of this dynamic optimization problem. Section 2.1 presents the motivation for the design tool, Section 2.2 illustrates the resulting three-dimensional surfaces derived from simulation data, and finally, Section 2.3 introduces the measurement-based Power Smith Tube.

#### *2.1: Motivation for 3D Search Space*

##### *2.1.1 Power Amplifier Background*

Many performance factors must be taken into consideration for the design and fabrication of a power amplifier. Among the most important considerations are the efficiency and linearity of the transmitting amplifier. A power amplifier's efficiency is

determined by its ability to convert DC electrical energy into amplifying the RF input signal. High efficiency is desirable since energy that is not transferred to the input waveform is dissipated in other forms such as heat, which in turn decreases the performance of the amplifier. The metric used for efficiency in this paper will be the power-added efficiency (PAE). Equation 2.1 demonstrates how the PAE of an amplifier is calculated:

$$PAE = 100 \times \left[ \frac{P_{out,RF} - P_{in,RF}}{P_{DC}} \right] \quad (2.1)$$

Where,  $P_{out,RF}$  is the total power contained in the output signal,  $P_{in,RF}$  is the total power contained in the input signal, and  $P_{DC}$  is the total DC power used to bias the amplifier's transistor.

An amplifier that is said to have high linearity will effectively increase the amplitude of the input signal without altering or distorting the content of the signal. For audio amplifiers this is analogous to a signal's fidelity. Nonlinearity can manifest itself by causing the amplifier's transmitted output signal to spread into adjacent channels due to third-, fifth-, seventh-, and other odd-order intermodulation distortion. Adjacent-channel power ratio (ACPR) is the ratio of a signal's total adjacent channel power to the signal's main channel power. The calculation of ACPR can be seen in equation 2.2 where ACPR is the logarithmic ratio of the measured powers, and as a result is referred to in units of dBc (decibels relative to the carrier). It can be noticed from equation 2.2 that when ACPR is calculated to be negative, then by definition the adjacent channel signal strength is less than the main channel signal strength. Therefore, the lower the ACPR, the more linearly an amplifier behaves.

$$ACPR = 10 \log_{10} \left( \frac{P_{adjacent}}{P_{main}} \right) \quad (2.2)$$

The purpose of ACPR is to provide a quantitative figure-of-merit for side lobes or spectral regrowth. Common uses of ACPR involve determining the effect a signal operating in its allocated frequency range has on neighboring frequency ranges. In a now crowded electromagnetic spectrum, ACPR has become a very important design criterion for RF signal operation. Figure 2.1 depicts the effect an increase in ACPR has on neighboring frequencies. As the amplifier is driven into more nonlinear operation, the spectral regrowth increases, which also increases the ACPR.

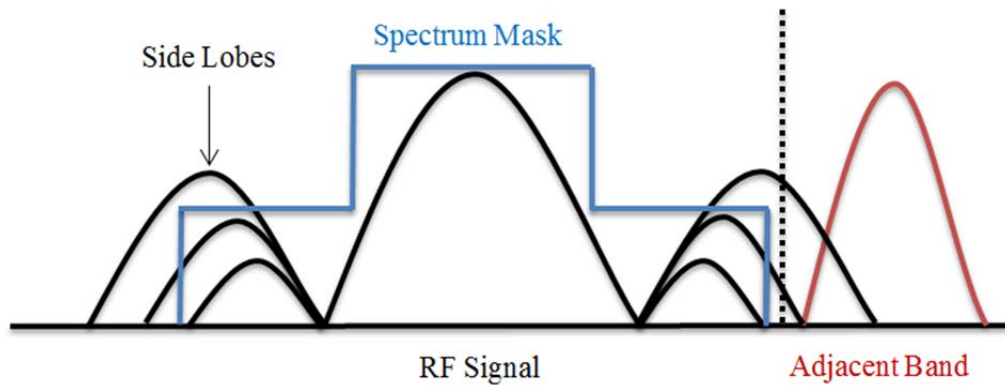


Figure 2.1: Demonstration of the effects decreased linearity has on an operating signal. It can be seen that as the linearity decreases the side lobes or spectral regrowth increases causing the operating signal to reach into its neighbor's band.

Power amplifiers that are both highly efficient and linear have been shown to be important in design as shown by Hajji [1]. Achieving high efficiency as well as favorable linear performance has become a topic of recent interest due to the increasing use of signals with high peak-to-average power ratio (PAPR) in many wireless communication systems. RF power amplifiers have also been shown to produce an improvement in

efficiency and linearity when both the input power,  $P_{in}$ , and the load reflection coefficient,  $\Gamma_L$ , are varied to the point of achieving optimum efficiency [2]. Methods involving the use of varactor diodes to tune matching networks have been shown to improve a power amplifier's linearity as well as PAE by tuning for a desired dynamic load [3].

### *2.1.2 Previous Design Approach*

In typical power amplifier design, one parameter can be optimized at a time through the use of load-pull and power sweep measurements performed in repeated succession. A load-pull can be described as measurements of a performance criteria (such as PAE or ACPR) measured over a mesh of identically distributed measurements taken on a Smith Chart that, if dense enough, roughly characterize the dependence of the criterion over load-impedance variation at a given power level. This mesh can be seen in Figure 2.2, where roughly 298 measurements are used to create ACPR and PAE contours.

After the load-pull is performed, the complex load impedance with the most desirable characteristics is then chosen as the new operating point. This method of performing a load-pull for an efficient operating location has been shown to improve both the PAE and ACPR of RF power amplifiers in previous works [4]. Once the new operating load impedance is chosen, a power sweep is performed at the previously specified  $\Gamma_L$  to view the effect that changing the  $P_{in}$  has on the power amplifier design characteristics. Figure 2.3 below is a typical power sweep done using Maury ATsv5 software and a load tuner provided by Maury Microwave. Power sweeps can also be constructed in simulation using design software.

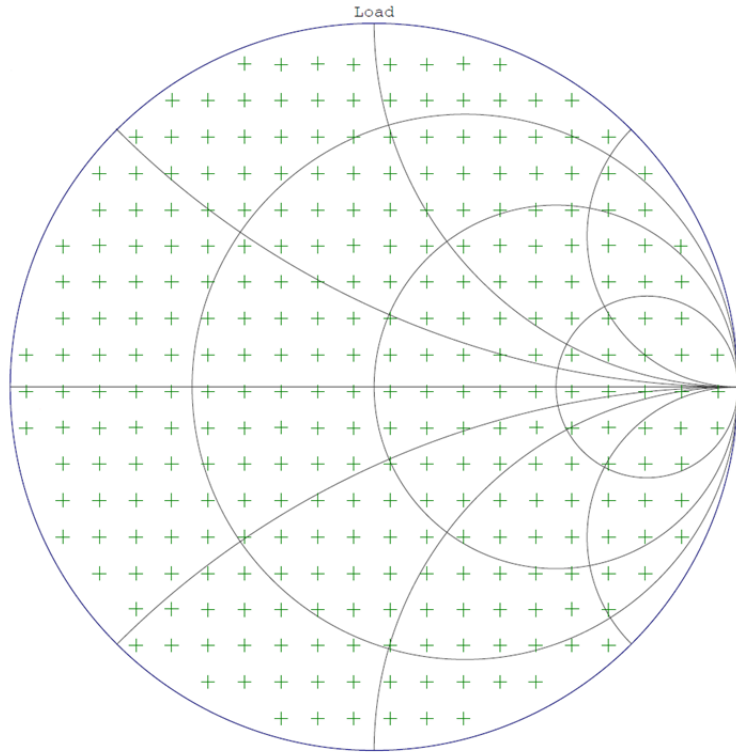


Figure 2.2: Example of a typical load-pull inside the Smith Chart with the green '+' symbols representing measurement points. In order to obtain accurate contours a dense set of measurements must be taken. The load-pull used in this examples takes around 30 minutes to complete with a load-tuner.

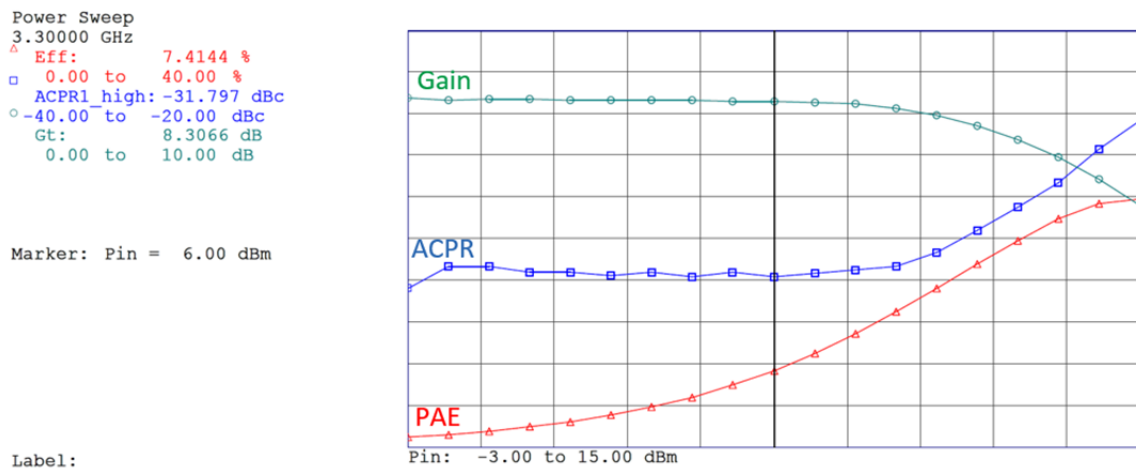


Figure 2.3: Measurement results of a power sweep done at:  $\Gamma_L = 0.0456 \angle 99.84^\circ$  using a Maury ATsv5 software. The change in PAE, ACPR, and gain over input power can be seen in red, blue and green respectively.

Notice in Figure 2.3 that as the input power increases, the device begins to go into compression near the input power level of 13 dBm. This is caused by nonlinearities in the amplifier when signals with large  $P_{in}$  are passed through the amplifier. Once the amplifier is in its compression region, it is noted that an increase in input power will not directly relate to a proportional increase in output power. This indicates nonlinear behavior, which will also lead to harmonic distortion of the output signal. Note the effect varying  $P_{in}$  has on both the efficiency and ACPR line plots. As mentioned earlier, as input power is increased, the signal's linearity decreases while the efficiency increases.

With the power sweep completed, the next step in the design process is to select the input power level that yields the most desirable constraint efficiency. With that new power level selected, another load-pull will be performed in order to view the landscape on the Smith Chart at the new power level. Then, the next ideal operating location is selected and another power sweep and load-pull is performed. This process continues until the designer is satisfied with the results of the amplifier's performance. The load-pull allows visualization of the efficiency and linearity behavior over varying load impedance, and the power sweep allows visualization of the efficiency and linearity behavior over varying input power. The need to use two different visualizations for the variations of load impedance and input power makes it difficult to fully understand the combined effect of load impedance and input power on efficiency and linearity. The Power Smith Tube provides a solution to this problem.

### *2.1.3 Prior Art*

Since the creation of the world's first amplifying vacuum tube in 1906, amplifier optimization has been a focus of constant development [5]. It was not until the early 1970's that the idea of adaptive radar arose to meet the need for improving radar performance [6]. With the current shortage of available spectrum, wireless transmitting amplifiers need to become more spectrally aware through the use of reconfigurable circuitry. Much has been done recently in signal processing to improve the performance of adaptive radar applications [7,8,9,10]. However, it is important to note that the work presented in this thesis will pertain primarily to the reconfiguration of RF circuit parameters rather than signal processing.

The variation of the circuit parameters; load impedance, input power, and biasing voltages have been shown to significantly affect power amplifier performance [11]. Real-Time impedance tuning through the use of MEMS switches [12,13], varactors [3], and resonant cavities [14] have been proven to directly benefit power amplifier design. Additionally, signal input power has been well-documented to improve power amplifier efficiency at a variety of load impedances [2,15]. Literature has also shown that a power amplifier's biasing conditions are directly correlated to efficiency and linearity [16,17].

Genetic algorithms have been proposed as a method to tune these circuit parameters in real-time [18]. However, these genetic algorithms are predicted to be slow in tuning for many applications [19]. A paper published by Baylor Wireless and Microwave Circuit and Systems (WMCS) demonstrates quick optimization of circuit parameters [20] with the goal of improving amplifier efficiency with a given linearity constraint. The purpose of the present work is to show how an optimum combination of

load impedance, input power and biasing voltage can be obtained quickly using a minimal number of experimental queries through a fast search algorithm. The optimization trade-off of efficiency and linearity is an example of a bi-objective optimization [21,22]. This consideration is a type of Pareto optimization, in which multiple objective functions are optimized simultaneously [23,24,25,26].

## 2.2 *The Power Smith Tube*

The Power Smith Tube is a graphical aid for visualizing both PAE and ACPR while varying  $\Gamma_L$  and  $P_{in}$  easily in a three-dimensional search space. The Power Smith Tube is similar to the Smith Tube presented by Fellows [27], but the vertical axis is a representation of the input power rather than the bandwidth of a chirp waveform. This can be seen in Figure 2.4, where the Power Smith Tube is depicted with the Z dimension representing  $P_{in}$ , the input power of the input waveform. The Power Smith Tube can be conceptually constructed by stacking Smith Charts on top of one another, with each Smith Chart on the stack representing another unique input power level. The goal of the Power Smith Tube is to provide a means of visualizing the combined impact of load impedance and input power in a novel way.

This visualization tool can aid in the achievement of both high efficiency and ideal linearity performance, a design problem that has received considerable attention. The Smith chart has previously been extended in different ways to solve circuit design problems. Previous extensions allow visualization of negative impedances [28, 29], fractional circuit elements [30], and lossy transmission-line elements [31]. However, these previous extensions take the form of a sphere instead of a cylinder like in Figure 2.4.

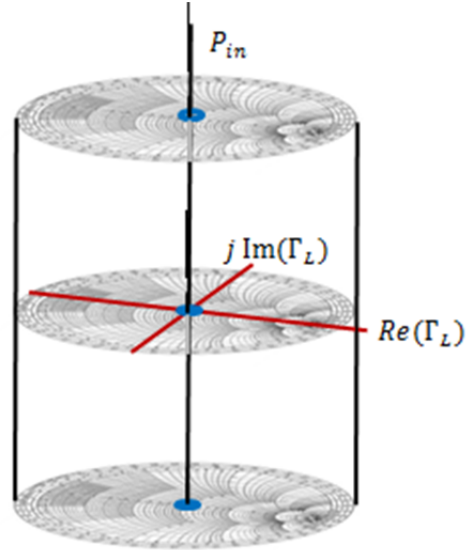


Figure 2.4: The Power Smith Tube. The vertical axis can be seen to represent the input power, while the horizontal cross section of the tube is the traditional Smith Chart reprinted from [20].

The Power Smith Tube presented allows the user to more easily find the combination of  $\Gamma_L$  and  $P_{in}$ , which together produce the largest power added efficiency (PAE) and the adjacent channel power ratio (ACPR) contours as a function of both  $\Gamma_L$  and  $P_{in}$ . In order to create the Power Smith Tube, load-pull measurements were performed to measure PAE and ACPR contours as a complex function of  $\Gamma_L$  at different levels of  $P_{in}$ . Within each power level the complex values of  $\Gamma_L$  that were found to meet the ACPR acceptable region were identified. Once all the measurements were taken, the measured point with the highest PAE which also met ACPR requirements can be chosen as the constrained optimum design point. Since both PAE and ACPR exhibit convex behavior, the constrained optimum of the combination of the sets will lie on the ACPR limiting surface that is tangent to the PAE surface. This is discussed by Martin for two-dimensional convex optimization where PAE and ACPR contours are co-linear on the

Pareto optimum locus [21]. This is based on the information that the three-dimensional convexity of the Power Smith Tube can be assumed, which may not be the case for every device. However, because the ACPR is the limiting constraint, it will likely force the PAE optimization to a useful solution that is near the global optimum, even in many cases where both the PAE and ACPR surfaces are not convex.

As shown in Figure 2.5, typical device power compression curves tend to show that PAE increases to a maximum, then drops off again as  $P_{in}$  continues to increase. Similarly, the PAE surface in the Power Smith Tube can be expected to behave in an identical fashion, but in three dimensions rather than two. In three dimensions, the PAE surface would widen as the input power is increased to its maximum point where the surface would then shrink as  $P_{in}$  is further increased. For ACPR, the linearity for a given  $\Gamma_L$  can be presumed to decrease as the input power is increased. This will result in a constant-ACPR surface that will narrow as the Power Smith Tube is ascended, with fewer values of  $\Gamma_L$  providing the minimum acceptable ACPR value. A two-dimensional power sweep graph is provided in Figure 2.5 to illustrate the effect input power has on PAE so that the concept can be better understood when translated to three dimensions.

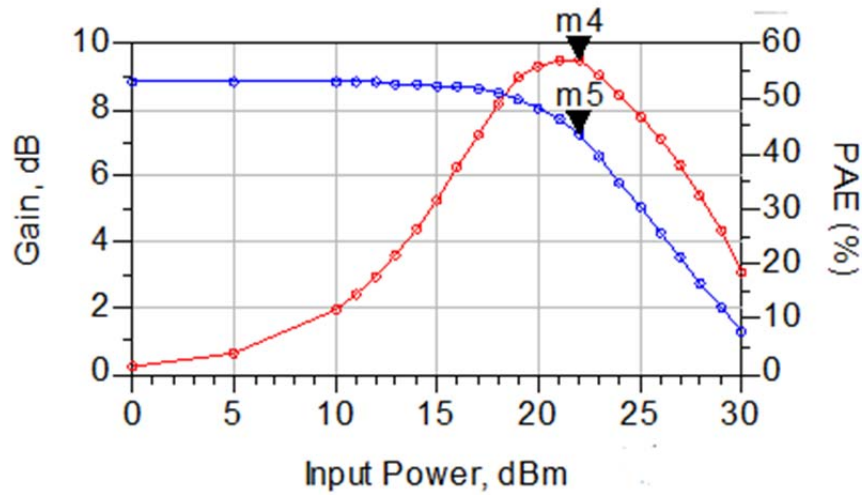


Figure 2.5: Graph representing the tradeoff of increasing the input power of a transmitter amplifier. When the input power of an amplifier is increased, the resulting effect is increased efficiency and decreased linearity. At points m4 and m5 the amplifier begins to be pushed into compression.

To create the PAE and ACPR characteristics in the Power Smith Tube, load-pull measurements were performed in simulations on a Nonlinear Gallium Arsenide FET (GaAsFET) model built in to the Advanced Design System Software (ADS) provided by Keysight Technologies. This device was then biased with a gate voltage  $V_{GS} = -1 V$  and a drain voltage  $V_{DS} = 5 V$ . The input signal used was a RF carrier modulated by a CDMA2K reverse-link signal at 825 MHz, which was also provided in the default design directories of ADS. Load-pull simulations were performed over input power levels ranging from 0 to 37 dBm with an imposed requirement of  $ACPR \leq -40 dBc$ . From the load-pull data taken over all input power levels, the maximum constrained PAE (given the ACPR limit) was found at an input power level of  $P_{in} = 21 dBm$  with  $\Gamma_L = 0.800 \angle 180^\circ$ , where the PAE was found to be 36.79%. Figure 2.6 displays load-pull contours generated from measurements at input power levels

of  $P_{in} = 20, 21, \text{ and } 22 \text{ dBm}$ . In these figures the ACPR acceptable region identified as  $\text{ACPR} \leq -40 \text{ dBc}$  is shaded in yellow and, as predicted, the ACPR region decreases in size as the input power of the input signal waveform is also decreased.

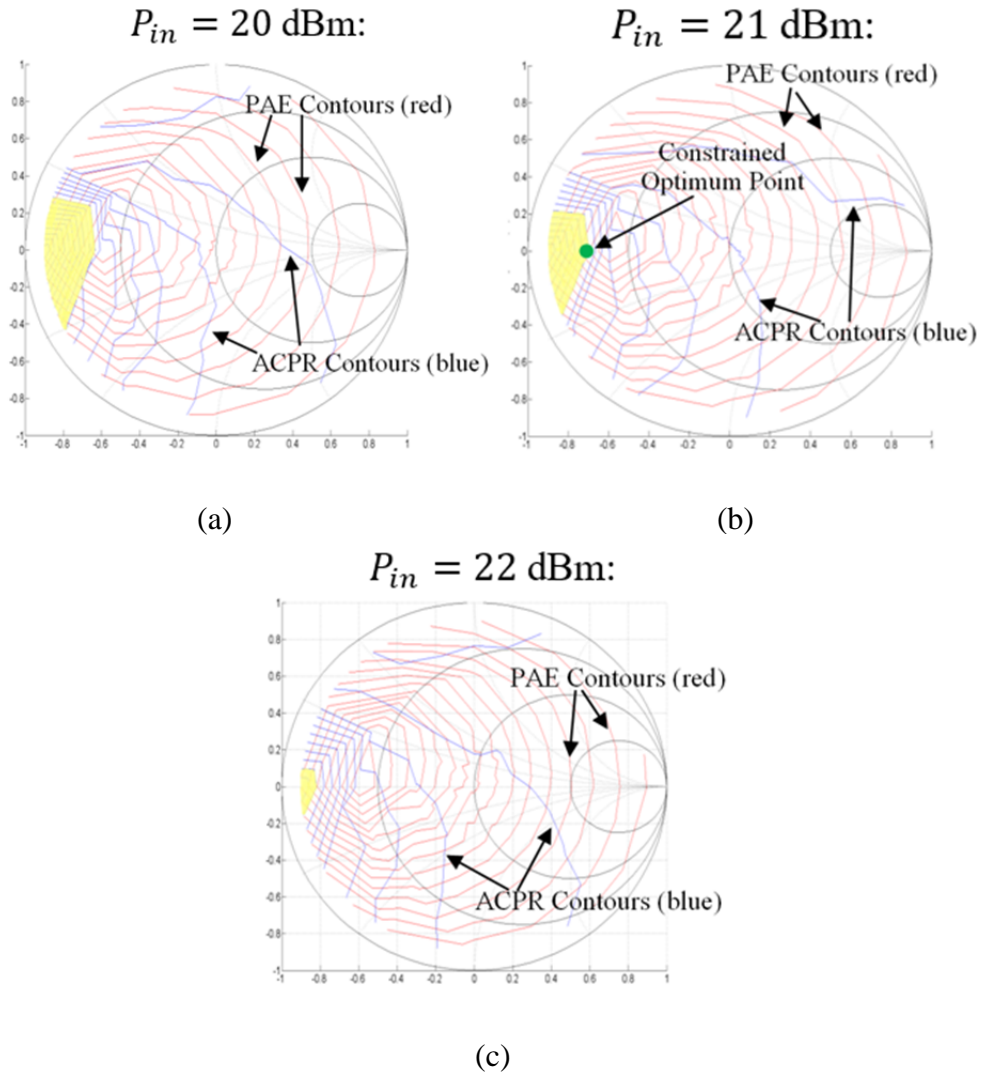


Figure 2.6: Load-pull simulations conducted at different power levels in simulation using ADS for a GaAsFET device. Graphs a, b, c correspond to power levels 20, 21, 22 dBm respectively. In graph (b) the constrained optimum point is found and exists at the tangential boundary of PAE and ACPR at the location  $\Gamma_L = 0.800 \angle 180^\circ$ .

The three load-pulls depicted above hint to what a three-dimensional ACPR surface would look like with the ACPR area decreasing as the input power is increased. It can be assumed that if these three plots were stacked on top of one another in order from lowest power level to highest power level, the three-dimensional surface of the highlighted region would look similar in shape to that of a stalagmite. Combining 7 sets of PAE and ACPR contours yields the graph seen in Figure 2.7.

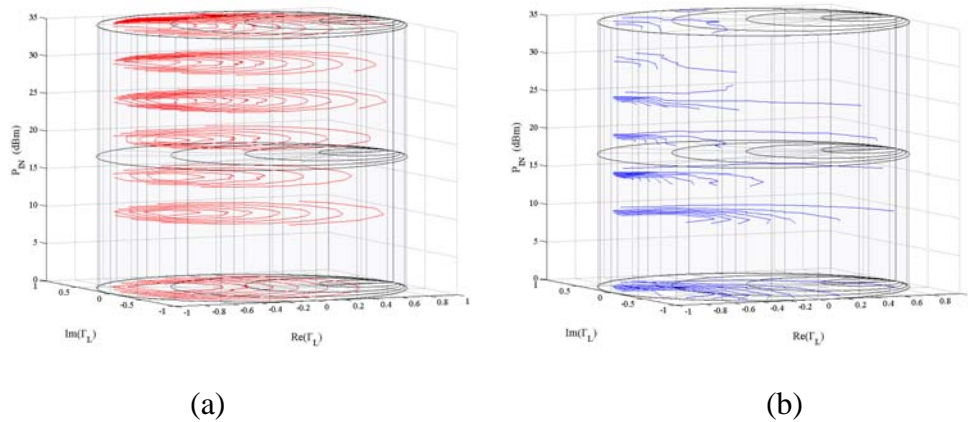


Figure 2.7: (a) Simulation results of PAE contours stacked on top of one another with each contour level representing the PAE at a different power level. (b) ACPR contours stacked on top of one another in the Power Smith Tube.

Building off of the idea of stacking ACPR and PAE contours in three-dimensions, a surface plot was created to display the acceptable region rather than individual contours. To create a three-dimensional surface plot, ADS load-pull data was fed to MATLAB where it was then formatted in accordance with MATLAB's plotting functions. Figure 2.8 shows the ACPR surface representing  $\text{ACPR} = -40 \text{ dBc}$  in the Power Smith Tube with the red surface above the ACPR surface representing  $\text{PAE} \geq 40.18\%$ , which is the value of the constrained global optimum PAE. It can be seen that the surfaces intersect at one point because they are tangent to one another, akin to Figure

2.6 (b) where the ACPR and PAE contours touch each other tangentially. This location represents the Pareto optimum locus in the set of  $(\Gamma_L, P_{in})$  points in which the optimum PAE is provided given the predefined constraints to ACPR.

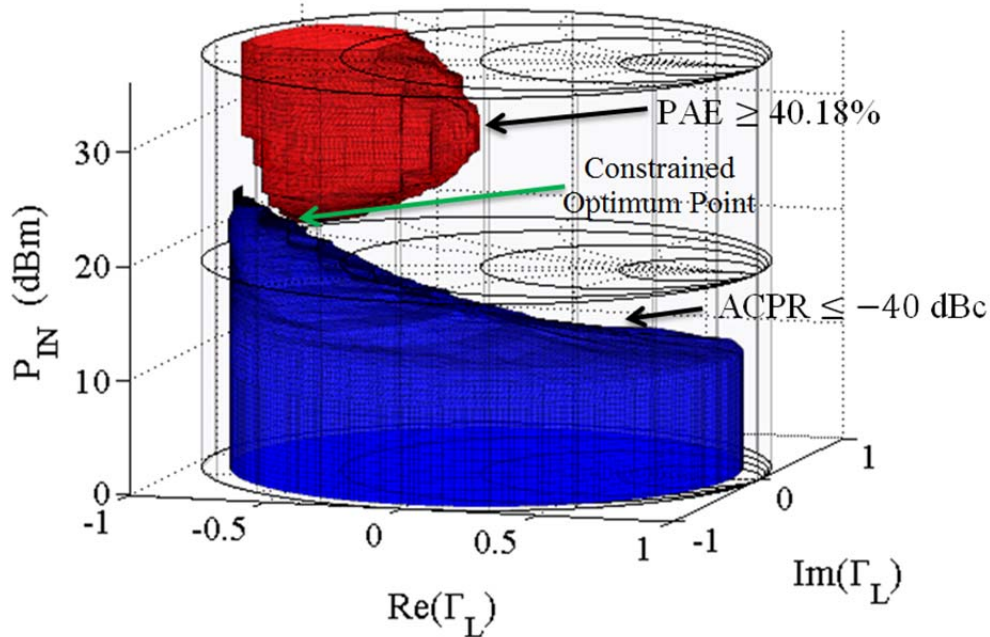


Figure 2.8: Constant ACPR surface created from simulated data for an ACPR limit of -40 dBc and the corresponding PAE surface representing the maximum PAE given the ACPR constraint. The constrained optimum location occurs where the two surfaces intersect; at this point, the two surfaces are tangent. The optimum location for this surface was found at  $\Gamma_L = 0.8 \angle 180^\circ$  and  $P_{in} = 21.75 \text{ dBm}$  where  $PAE = 40.18\%$  and  $ACPR = -40.23 \text{ dBc}$ . This surface plot was created using ADS built in models for a GaAs FET.

It can be seen in Figure 2.8 that the Power Smith Tube ACPR and PAE surfaces possess convex-like qualities. This, however, may not always be the case when dealing with alternate amplifiers. To test this theory, another device was used in the load-pull simulation software. A Modelithics Angelov model for a Qorvo TGF2960 GaAs Heterojunction field-effect transistor (HFET) was simulated in Keysight Technologies' Advanced Design System (ADS). The biasing conditions for this Modelithics model

were  $V_{GS} = -0.94$ ,  $V_{DS} = 8$  V, where the same CDMA2K signal was used with an RF frequency of 800 MHz in order to correspond with Modelithics measured datasheet. The red and blue surfaces seen in Figure 2.9 correspond with the PAE and ACPR contours varied at each power level.

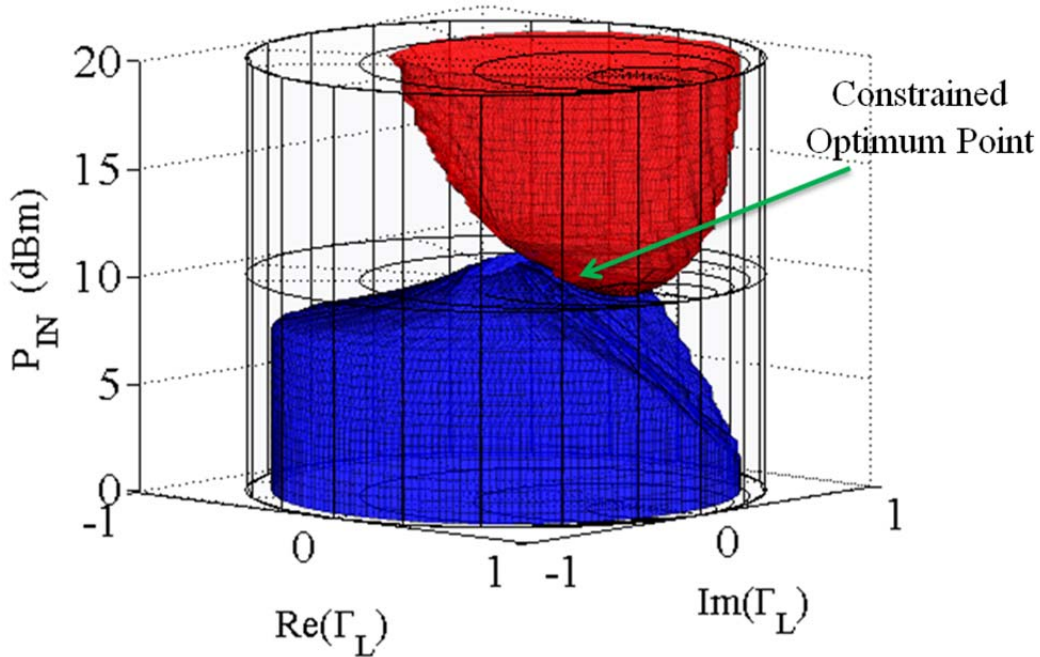


Figure 2.9: Constant ACPR surface created from simulated data for an ACPR limit of -50 dBc and the corresponding PAE surface representing the maximum PAE given the ACPR constraint. The constrained optimum location occurs where the two surfaces intersect; here at this point, the two surfaces are tangent. The optimum operating location of this device was found at:  $\Gamma_L = 0.25 \angle 80^\circ$  and  $P_{in} = 10$  dBm with an PAE = 34.96% and ACPR=-50.21 dBc. This surface plot was created using Modelithics ADS models for a TriQuint TGF2960 GaAs HFET device.

The PAE and ACPR surfaces in Figure 2.9 appear to be very similar to the surfaces in the ADS simulated model seen in Figure 2.8. In both of these created Power Smith Tubes, the ACPR surface in blue appears to lack complete convexity. The absence of complete convexity creates a problem for traditional optimization techniques because

the design could potentially land in a local maxima operating location rather than the global best. Fortunately, with the use of this particular Power Smith Tube, finding the global maxima is trivial. This is because the once complex nonlinear optimization can easily be visualized, the local maximums can also be avoided accordingly.

### *2.3 Power Smith Tube Measurement Results*

Creating a Power Smith Tube in a simulation environment has proven to be a beneficial tool that any power amplifier (PA) designer would appreciate. This same Power Smith Tube could also be considerably useful to present the load-impedance and input-power variations of measured PAE and ACPR on a datasheet for a commercial power amplifier or device. To create a Power Smith Tube plot based on measured data, multiple load-pull measurements on a SKY5017-70LF InGaP packaged amplifier were taken and used as a basis of characterization. The measurement test setup used to take these measurements can be seen in Figure 2.10.

A 3 GHz step function was generated in these measurements where a Power Meter and a Spectrum Analyzer were then used to measure the post-amplification output signal. Communication between the devices shown in Figure 2.10 was accomplished by using MATLAB in correspondence with Agilent and Maury communication functions. Full load-pulls taken at power levels from -5 dBm to 2 dBm in 0.5 dBm increments were performed in order to obtain a dense sample size for Power Smith Tube construction. The load-pull output files were then opened as .txt files and fed to MATLAB, where the information was reorganized to be of useful format for MATLAB's two and three-dimensional rendering functions.



Figure 2.10: Load-pull test setup involving a Maury Microwave automated tuner (MT982B), Agilent N5182A MXG vector signal generator, Agilent E3647A dual output DC power supply, Agilent N1911A P-Series power meter, and an Agilent E4407B ESA-E series spectrum analyzer.

Figure 2.11 shows the ACPR and PAE contours constructed from the load-pull measurements at power levels  $P_{in} = 0, 1,$  and  $2$  dBm. The user-defined ACPR constraint for this Skyworks packaged amplifier is  $-27.5$  dBc, which is shown as the highlighted region in Figure 2.11. This highlighted region illustrates all the acceptable operating  $\Gamma_L$  values for each individual power level. The load-pull taken at the power level  $P_{in} = 1$  dBm contains the constrained maximum PAE value. It is also important to note that although acceptable values of  $\Gamma_L$  exist at higher input power levels, the global constrained optimum PAE is not found at the highest power level for which an acceptable-ACPR region exists. In this example, the optimum is found at one power level lower. This is because the PAE contours for this device are located more towards the center of the Smith chart rather than on the right side where the ACPR contours originate. This leads to the design problem discussed earlier in which decreasing linearity aggressively affects the operating efficiency of the power amplifier.

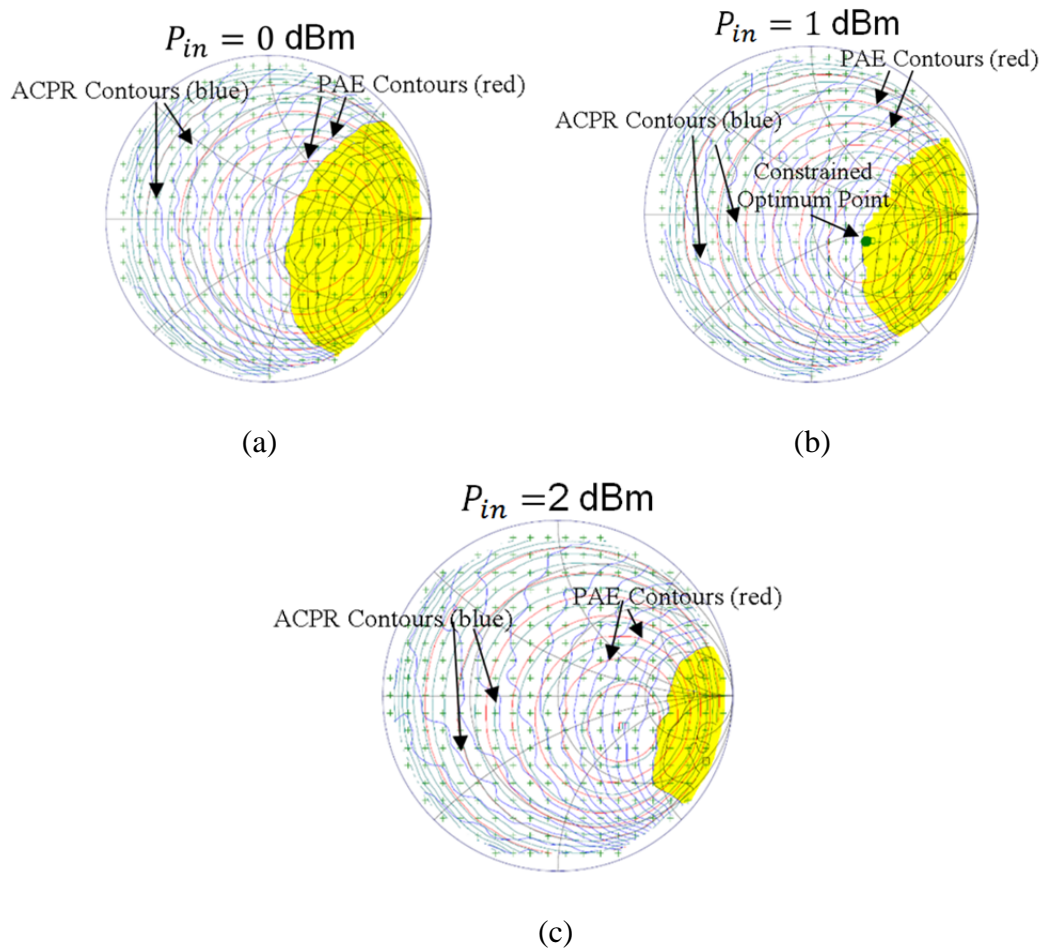


Figure 2.11: Measured PAE and ACPR load-pull contours at  $P_{in}$  levels (a) 0 dBm, (b) 1 dBm, and (c) 2 dBm. The highlighted yellow region is the acceptable ACPR region ( $ACPR \leq -27.5 \text{ dBc}$ ) where the constrained optimum point is found at power level  $P_{in} = 1 \text{ dBm}$  or figure (b).

The ACPR contours seen in Figure 2.11 depict an analogous result that is seen in the load-pull slice view for simulation data in Figure 2.6. In both devices, in simulation and measurement, ACPR decreases as input power is increased, whereas PAE increases. Unlike in simulation, load-pull measurements for the Skyworks DUT were not taken at higher power levels for fear of damaging the packaged amplifier. Operating the Skyworks DUT at high power levels in regions with poor efficiency leads to energy being dissipated elsewhere in the device. The main form the dissipated energy takes is heat,

which could destroy the DUT or cause it to no longer behave as intended. As such, the Power Smith Tube was capped at the input power of 2 dBm. Since the amplifier was not pushed any higher, the bulb shape of the PAE surface cannot be seen in the Power Tube for the measured device. However, the PAE shape is not needed because the only constraint imposed is an ACPR limit. The design goal is to maximize the PAE of the device at any given ACPR limit, therefore, nothing over the limit is useful.

Remarkably, the Power Smith Tube's ACPR surface for the Skyworks DUT seen in Figure 2.12 shares similar characteristics with that of the Power Smith Tube generated in previous simulation results. As explained earlier, this is expected, as linearity generally decreases with increasing input power. In order to confirm these findings in measurement, another Power Smith Tube was created for a different device. To create the Power Tube seen in Figure 2.13 a total of 17 load-pulls were performed on a MWT173 GaAs MESFET.

Both of the ACPR surfaces seen inside the Power Tube in Figures 2.12 and 2.13 show great correspondence. Since the ACPR contours on both devices originate on different sides of the Smith chart, it follows that the resulting ACPR surfaces for each device would fade off in different directions of the Power Tube. It can now be assumed that most power amplifiers have an ACPR surface that is some permutation of the surface in Figure 2.12. With this precedence realized, future power amplifier design can now be refreshed with new and innovative solutions.

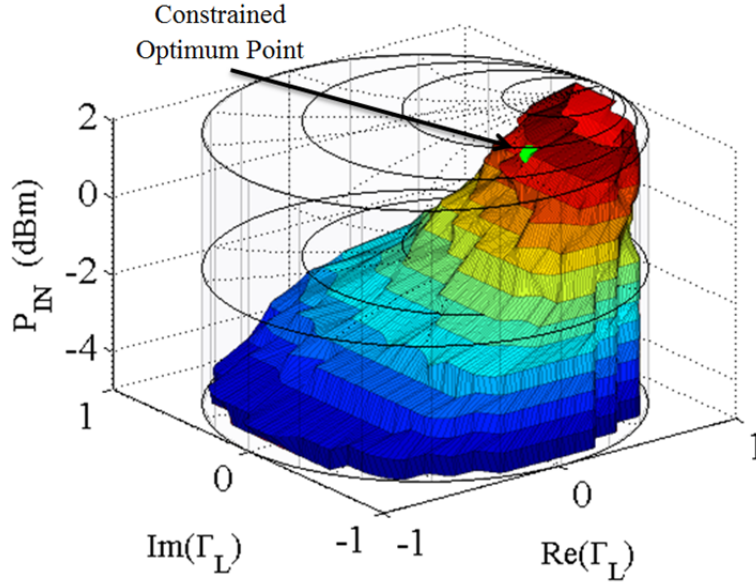


Figure 2.12: ACPR surface inside the Power Smith Tube with the constraint of  $ACPR \leq -27.5$  dBc. The DUT used in measurement was a SKY5017-70LF InGaP packaged amplifier. The constrained optimum PAE value 7.39% was found at the operating location of  $\Gamma_L = 0.35\angle -28.4^\circ$  at an input power of  $P_{in} = 1.5$  dBm which can be seen as a green circle on the edge of the surface.

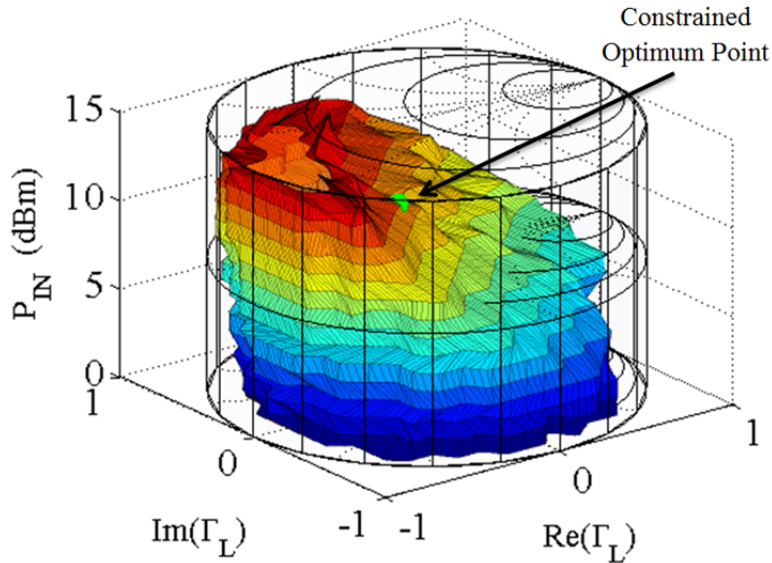


Figure 2.13: The ACPR surface inside the Power Smith Tube for a Microwave Technologies MWT-1 GaAs MESFET chip. The biasing conditions used for this Power Tube were:  $V_{GS} = -1$  V,  $V_{DS} = 4.5$  V. The constrained optimum location was found at:  $\Gamma_L = 0.316\angle -148.77^\circ$  with a  $P_{in}=12$  dBm where the PAE = 20.58% and  $ACPR = -30.05$  dBc.

## *2.4 Summary*

A novel tool has been proposed that allows for a new way of visualizing a classical power amplifier design problem. The practicality in application has been shown for an ideal simulation, model simulation, and measurement environments. The Power Smith Tube can be used as a means to spark new and creative optimization techniques and algorithms. These innovative techniques can be further developed to improve speed and accuracy as well as decrease the difficulty of future design.

## CHAPTER THREE

### Fast Optimization in the Power Smith Tube

In the previous chapter, a novel visualization tool, termed the Power Smith Tube, was presented as a means to view the dynamic optimization problem faced in power amplifier design. This chapter describes a new search technique, using the Power Smith Tube as the search space, to simultaneously optimize the load impedance and the input power in order to maximize the efficiency while also meeting spectral constraints quickly. Section 3.1 discusses the theory and mathematics involved in this gradient-based search algorithm. Section 3.2 demonstrates the search's effectiveness in both measurement and simulation examples. Section 3.3 discusses the use of momentum to improve search performance in noisy measurement scenarios, and finally, Section 3.4 summarizes the results.

#### *3.1 Motivation for a Search Algorithm*

The power amplifier is a critical component of communication and radar transmitters. Multiple objectives and tradeoffs for simultaneous optimization are considered in optimizing power amplifier performance. Variation of both the input power ( $P_{in}$ ) and load reflection coefficient ( $\Gamma_L$ ) significantly affects the linearity and efficiency of power amplifiers. Ubostad has shown that choosing optimal loading conditions of a power amplifier is required for achieving a high performance design [32]. The variation of both  $\Gamma_L$  and  $P_{in}$  results in a complex design surface with multiple objectives in a three-dimensional space [33].

With increasingly stringent spectral constraints, the adaptability of future radar transmitters is vital. These adaptive transmitters will need to reconfigure in order to allow operation in different frequency bands while meeting the various spectral constraints based on nearby wireless activity. Transmitters will have to quickly change their frequency of operation, transmission spectra, and circuitry to operate in the dynamically changing spectral environment while maintaining excellent performance and efficiency. These adjustments will need to occur on the order of milliseconds to be practical in real time.

Reconfiguring a load impedance tuner to improve a power amplifier's operating characteristics has been utilized in previous works. Okada has shown the usefulness of dynamically reconfigurable architecture for amplifier design by demonstrating the idea of multi-band RF circuits for Software Define Radio [34]. Lu utilizes shunt MEMS switches as capacitive stubs for adaptive matching networks [12]. Similarly, Vaka-Heikkila creates a reconfigurable matching network based on a loaded-line technique [13]. Deve presents an impedance tuner that can adjust its operating frequency between 1 and 3 GHz, a frequency range used for many wireless sensing applications [35]. The importance of intelligent impedance matching with minimized tuning iterations for reconfigurable transmitters is predicted by Sun [36].

Recently, reconfigurability has been implemented in the form of genetic algorithms controlling tunable MEMS circuits in order to improve power amplifier performance [37]. However, du Plessis predicts that genetic algorithms will be slow in tuning for many applications [19]. Previous work in impedance tuning has been primarily performed for communication applications, but Baylis describes the importance of

reconfigurable power amplifiers in solving the radar-communication problem of coexistence [38]. The idea of reconfigurable circuitry is relatively new in the radar domain; most of the previous radar optimization work focuses on optimizing the waveform. A recent development in radar is the design of adaptive waveforms and circuits that can reduce transmitter distortion while optimizing power efficiency and linearity. Polyphase-coded frequency-modulation (PCFM) waveforms are used for high power efficiency and spectral performance by Blunt [21]. Blunt also goes on to present the optimization of transmitter amplifier distortion through the use of these PCFM waveforms [22].

The Power Smith Tube previously presented can be employed as a visualization tool for optimization of power amplifier load reflection coefficient  $\Gamma_L$  and the input power  $P_{in}$  simultaneously. However, collecting the data to plot surfaces of equal efficiency and linearity throughout the Power Smith Tube requires a considerable amount of time. Effective use of this optimization tool would require a fast search algorithm to find the optimum combination of  $\Gamma_L$  and  $P_{in}$ . To use the Power Smith Tube for design without a fast search algorithm, multiple load-pulls at different input power levels can be performed in order to create three-dimensional surfaces of equal power-added efficiency (PAE) and adjacent-channel power ratio (ACPR). In particular, to collect the data for plotting surfaces of constant ACPR and PAE for the aforementioned nonlinear GaAsFET model in Keysight Technologies' Advanced Design System (ADS), a total of 37 load-pull simulations were performed at varied power levels. At each power level the load-pull simulation was performed with a total of 490 measurement points. By combining the 490 measurements for 37 load-pulls it can be seen that a total of 18,130 measurements were

used to create the three-dimensional PAE and ACPR surfaces seen in Figure 2.8. Even with significant computational strength, the sheer number of experimental queries required in an exhaustive measurement may be impractical for design use. Significant time and resources would be needed to fully mine all the data necessary for a particular problem. The Power Smith Tube is not merely a data presentation mechanism, but also a visualization tool to aid in developing new fast search techniques for power amplifier design and real-time optimization.

A new method for simultaneously optimizing the load impedance and the input power is presented in this chapter to improve efficiency and linearity in real-time. This search algorithm is designed for real-time optimization, enabling the joint reconfiguration of load impedance and input power of an adaptive communication and radar transmitter amplifier. Therefore, a main goal of the algorithm design is to minimize the number of experimental queries. This is an example of bi-objective optimization [21, 40], however, here it is applied to the well-known tradeoff between linearity and efficiency [11,41]. Optimization for linearity and efficiency using only the real and imaginary parts of  $\Gamma_L$  has been proven possible in previous works [42]. The aim of this chapter is to extend the optimization of  $\Gamma_L$  into a third-dimension and allow for the simultaneous optimization of input power and  $\Gamma_L$  to provide the highest PAE possible while also considering ACPR constraints.

### 3.2 Gradient-Based Search

The search algorithm unfolds based on PAE and ACPR gradient estimation measurements taken inside the three-dimensional input-power Smith Tube. To ensure that both  $\Gamma_L$  and  $P_{in}$  are given equal consideration in the search, the input power, which is the vertical axis of the Smith Tube, is normalized. The user-defined maximum input power is assigned the value of 1 and the user-defined minimum input power is assigned the value of -1. This normalization scales the vertical limitations of the cylindrical search space to be the same dimensions as the planar  $\Gamma_L$  magnitude limitation of the Smith Chart. The normalized input power  $p_{in}$  can be defined as follows:

$$p_{in} = 2 \frac{P_{in} - P_{in,min}}{P_{in,max} - P_{in,min}} - 1 \quad (3.1)$$

The purpose of normalizing the input power  $p_{in}$  is for its future use in the calculation and evaluation of gradients.

While the Power Smith Tube is limited to a cylindrical space, the search vectors and gradients can be formulated in Cartesian dimensions for the sake of simplicity. In this case the Cartesian coordinates; x, y and z are mapped to  $Re(\Gamma_L)$ ,  $Im(\Gamma_L)$ , and  $P_{in}$  values, respectively. Through the use of Cartesian coordinates the three-dimensional search becomes a direct extension of the search space used in the two-dimensional algorithm with the same objectives demonstrated by Fellows [27].

In order to move an operating location in the Power Smith Tube a search vector,  $\vec{v}$ , may be added to the current location or candidate point in order to find the subsequent candidate location in the search. In many design problems it is important that the resulting waveform meet spectral requirements. Therefore, it makes sense to prioritize the spectral requirements in real time due to the nature of this specification. It then follows

that when the search does not possess an acceptable ACPR value the resulting search vector is defined as follows:

$$\vec{v} = \hat{a}D_a + \hat{b}D_b, \quad (3.2)$$

where

$$D_a = \frac{D_s}{2} \frac{|ACPR_{meas} - ACPR_{target}|}{|ACPR_{worst} - ACPR_{target}|} \quad (3.3)$$

and

$$D_b = \frac{D_s}{2} \frac{|\theta_{meas} - \theta_{target}|}{\theta_{target}} \quad (3.4)$$

In equation 3.2, both  $\hat{a}$  and  $\hat{b}$  represent unit vectors in the direction of ACPR's steepest descent and the bisector angle between the ACPR's steepest-descent and PAE's steepest-ascent vectors. An example of how the gradients are calculated can be seen in Figure 3.1 below. The gradient for the PAE and ACPR is given in terms of the unit coordinate vectors  $\hat{\Gamma}_r$ ,  $\hat{\Gamma}_i$ , and  $\hat{P}_{in}$  by

$$\nabla p = \hat{\Gamma}_r \frac{\partial p}{\partial \Gamma_r} + \hat{\Gamma}_i \frac{\partial p}{\partial \Gamma_i} + \hat{P}_{in} \frac{\partial p}{\partial p_{in}} \quad (3.5)$$

$$\nabla a = \hat{\Gamma}_r \frac{\partial a}{\partial \Gamma_r} + \hat{\Gamma}_i \frac{\partial a}{\partial \Gamma_i} + \hat{P}_{in} \frac{\partial a}{\partial p_{in}} \quad (3.6)$$

The gradients in equations 3.5 and 3.6 are calculated from partial derivatives. The partial derivatives are estimated by measuring PAE and ACPR at a neighboring-point distance  $D_n$  from the current operating location in the Power Smith Tube. This neighboring step partial derivative calculation is depicted in Figure 3.1. The measured change in PAE,  $\Delta p$ , with respect to the load reflection coefficient's components,  $\Gamma_r$ ,  $\Gamma_i$ , and input power  $p_{in}$  follows as:

$$\frac{\partial p}{\partial \Gamma_r} \approx \frac{\Delta p}{\Delta \Gamma_r} = \frac{\Delta p}{D_n} \quad , \quad \frac{\partial p}{\partial \Gamma_i} \approx \frac{\Delta p}{\Delta \Gamma_i} = \frac{\Delta p}{D_n} \quad , \quad \frac{\partial p}{\partial p_{in}} \approx \frac{\Delta p}{\Delta p_{in}} = \frac{\Delta p}{D_n} \quad (3.7)$$

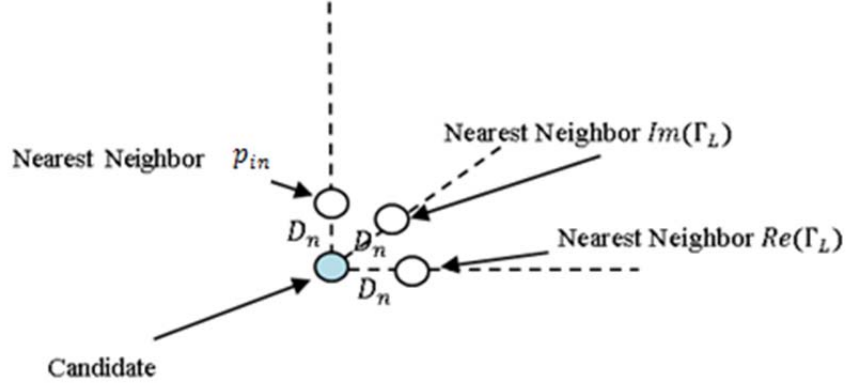


Figure 3.1: Gradient evaluation in three dimensions where  $D_n$  represents the neighboring distance step size, reprinted from [20].

The ACPR gradient used in the search vector is calculated similarly to equation 3.7 where each partial is measured at the corresponding neighboring point. Because it is desirable for ACPR to be minimized, the direction of optimal travel is given by the unit vector  $\hat{a}$  oriented in the direction of steepest-descent for the ACPR gradient.

$$\hat{a} = -\frac{\nabla a}{|\nabla a|} \quad (3.8)$$

The three-dimensional bisector of  $\hat{a}$  and  $\hat{p}$  can be defined as the arithmetic mean of the vectors  $\hat{p}$  and  $\hat{a}$ . Because  $\hat{a}$  and  $\hat{p}$  are both in unit vector form, the bisector can be given by

$$\hat{b} = \frac{1}{2}(\hat{a} + \hat{p}) \quad (3.9)$$

When the current operating location of the search is within ACPR compliance, the spectral requirements are met, but, the PAE likely is below its constrained optimum value. Due to this, the search can now focus on optimizing the PAE of the amplifier. This

can be interpreted as the substitution of the bisector component found in equation (3.2) by the PAE unit vector  $\hat{p}$  seen as

$$\vec{v} = \hat{p}D_a + \hat{b}D_b \quad (3.10)$$

Figure 3.2 illustrates the resulting search vector for the cases in which the ACPR at the current candidate is in compliance (Figure 3.2(a)) and when the ACPR at the present candidate is out of compliance (Figure 3.2(b)). From this figure it can be seen that when the search is operating outside of the ACPR compliance region the search dedicates its first step in the direction of ACPR compliance.

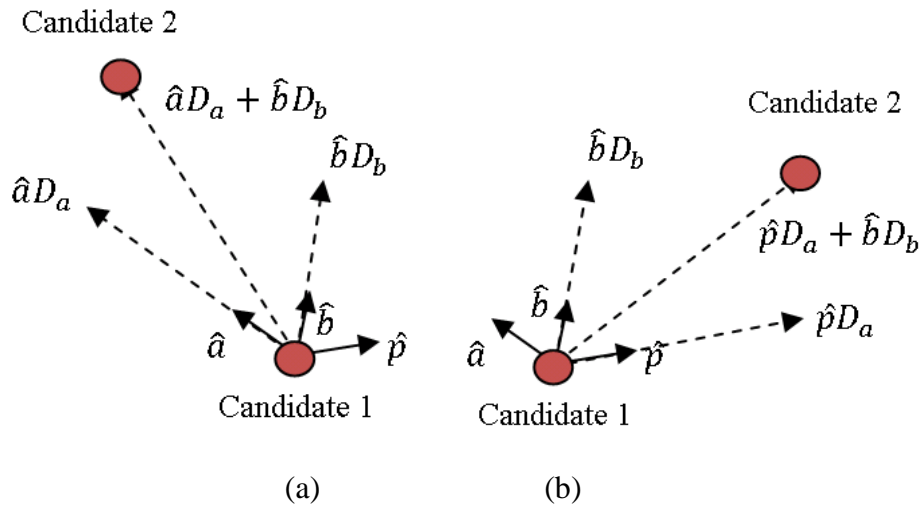


Figure 3.2: Search vector logic in two dimensions for the cases where (a) ACPR is not within constraints and (b) ACPR is within constraints, reprinted from [20].

Once the search is inside the acceptable ACPR region the search begins to progress towards the optimum PAE as long as the current operating location remains in compliance. This multi-objective movement can be noted in results presented in the following section, particularly when the search starts outside the region of compliance. The step towards ACPR's compliance region is generally seen predominantly as a

negative z-direction step due to steep  $P_{in}$  gradients. This negative z-direction step agrees with power amplifier (PA) design theory's suggestion that lower input power levels hold high linearity or, in other words, lower ACPR.

The search begins to converge toward an optimum solution when the search vector size decreases. Through equation 3.4 the search has the ability to recognize that it is near the Pareto optimum location. This is because the  $\theta_{target} = 90^\circ$ , where an angle of  $90^\circ$  indicates that both the PAE and ACPR vectors are perpendicular to each other. Therefore, as the search's bisector angle ( $\theta_{meas}$ ) nears  $90^\circ$ , the search vector will decrease as the numerator of equation 3.4 moves toward zero. Not only does the search's step decrease due to vector calculations, but the search also decreases if it is not able to find a superior operating location. Once the search is in the acceptable-ACPR region, the step size parameter  $D_s$  is halved if the search's next candidate point possesses worse PAE or an ACPR above the constraint limit. The step size will continue to be reduced by a factor of two until the search's next candidate point obtains a higher PAE or an ACPR that is below the constraint limit. The reduction of step size is implemented as a means to prevent the search from moving past the global optimum by assisting convergence. The search finally converges on a solution when the current vector step falls below the resolution distance threshold predefined by the user.

The gradient-based search approach presented is guaranteed to find the global optimum only in the case of Zadeh convexity, which exists if any line drawn between two points within a level set will also be within the level set at all locations [43]. In the previous chapter it has been seen that the two-dimensional PAE contours generated from load-pulls are typically convex. In many cases encountered in practice, the ACPR

contours in two dimensions also exhibit traits reasonably close to convexity, although in some cases (as noted previously) ACPR is not always convex.

However, when the Power Smith Tube is constructed in three dimensions, Zadeh convexity is less likely to occur. The surfaces generated in the Power Smith Tube represent the ACPR and PAE values of equality, but these sets may or may not possess the convexity Zadeh describes. From the power sweep generated in Figure 2.3 it can be seen that while the  $\Gamma_L$  is held constant, the second derivative of the PA efficiency remains positive as the input power is increased. The region of  $\Gamma_L$  values possessing equal PAE is expected to vary in radius in three dimensions with the increase of input power in the same fashion that the constant- $\Gamma_L$  PAE increases in a power sweep. This observation points to the belief that by connecting eqi-PAE contours in ascending order the resulting surface will vary in radius in a non-convex fashion. This non-convex characteristic could temporarily mislead the search. It seems based on our initial results, however, that the search will usually persist to successfully locate the constrained optimum, although non-convexities may cause an increase in measurements. This inference is reinforced by simulation and measurement results presented in the next section.

### *3.2.1 Simulation Results*

The algorithm was first implemented in simulations using a Nonlinear Gallium Arsenide FET (GaAsFET) built in to the Advanced Design System software (ADS) provided by Keysight Technologies. This same device was used in the previous chapter to generate the Power Smith Tube plot seen in Figure 2.8, where the maximum PAE providing  $\text{ACPR} \leq -40$  dBc was 40.18% found at  $\Gamma_L = 0.800 \angle 180^\circ$  and  $P_{in} = 21.75$  dBm.

In order to perform a fully automated search, a combination of both ADS and MATLAB software was used. MATLAB is used to query the user's search conditions such as starting location, step size, and search range. Then, the gradient calculations are performed in MATLAB. In order to obtain operating data about the amplifier, a netlist file was created that contains the software syntax necessary to describe the circuit schematic created for measurement using ADS' user interface (UI). This netlist was edited in MATLAB continuously to move the location being measured for future candidate locations as well as for taking neighboring gradient measurements. In order to simulate the created netlist file, a Windows command line prompt was employed to invoke the ADS co-simulator and point to the desired netlist to be simulated. Finally, the output of the simulation is stored in a MATLAB friendly format so that MATLAB could import the simulation output data and the appropriate calculations could be made for the next objective of the search.

The simulated algorithm tests were performed using a step size of  $D_s = 1$ , and a neighboring point distance of  $D_n = 0.05$  with an input power range of  $0 \text{ dBm} \leq P_{in} \leq 36 \text{ dBm}$ . Both the step size and neighboring point distance  $D_n$  and  $D_s$  have units consistent with the dimensions of the Smith Chart and are therefore unit-less. The step size and the neighboring point distance were the same for the five searches shown below in order to illustrate the robustness of the search.

Figure 3.3 shows the trajectory of a search starting from  $\Gamma_L = 0.5 \angle 90^\circ$ ,  $P_{in} = 5 \text{ dBm}$ . For this search a total of 29 measurement points were required in order for the search to converge on an optimal solution location of  $\Gamma_L = 0.79 \angle -178.6^\circ$  and  $P_{in} = 21.58 \text{ dBm}$ . At this location,  $\text{PAE} = 41.13\%$  and  $\text{ACPR} = -40.08 \text{ dBc}$  were obtained.

Figure 3.4 also illustrates the search trajectory for the starting point of  $\Gamma_L = 0.90\angle 0^\circ, P_{in} = 0$  dBm. Even though the starting points in both of these searches differed, the endpoint values of  $\Gamma_L, P_{in},$  PAE and ACPR are very similar. This similarity indicates that both of these searches converge to nearly the same location in the Power Tube.

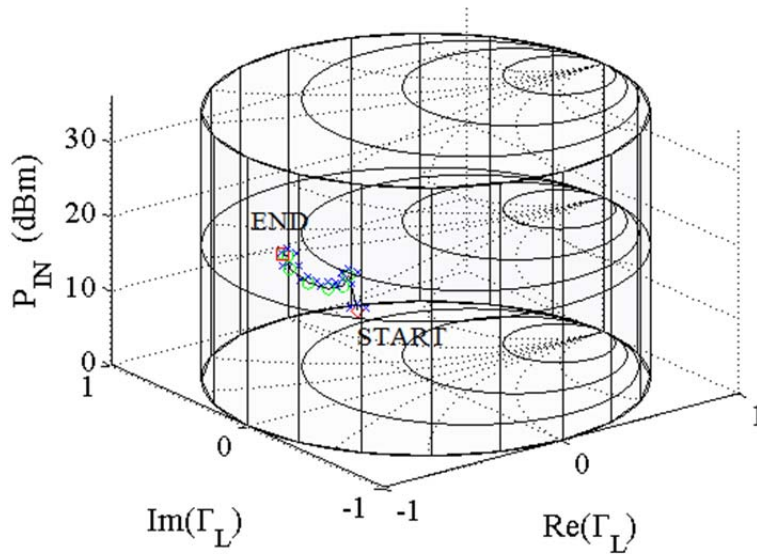


Figure 3.3: Simulated search algorithm trajectory through the Power Smith Tube with parameters;  $D_s = 1$ , input power range  $0 \text{ dBm} \leq P_{in} \leq 36 \text{ dBm}$  and a starting location  $\Gamma_L = 0.50\angle 90^\circ, P_{in} = 5$  dBm. The search required 29 measured points and converged to the endpoint  $\Gamma_L = 0.79\angle -178.6^\circ$  and  $P_{in} = 21.58$  dBm, where PAE = 41.13% and ACPR = -40.08 dBc.

Figures 3.5 through 3.7 depict search results for the additional starting combinations of  $\Gamma_L$  and  $P_{in}$ . Table 3.1 summarizes the results for these different starting combinations in simulation. In the results it can be seen that the final values of PAE vary by less than 1%, and that the ending ACPR values are all within 0.2 dB of the -40 dBc limiting value. This is also noted in the actual graphical location of the endpoints; where both the  $\Gamma_L$  and  $P_{in}$  coordinates vary slightly with the variation of  $P_{in}$  being less than 1 dB. The search results are also confirmed by the exhaustive load-pull searches performed

in the last chapter in order to create the Power Smith Tube. Through the extensive load-pull search the optimum was found at location  $\Gamma_L = 0.80\angle 180^\circ$  at a power level of 21.75 dBm, where PAE = 40.18% and ACPR = -40.23 dBc. Even with the increased density of the load-pull search, the PAE values obtained from the algorithm are all slightly better than the optimum obtained. This is because the points used to create the Power Smith Tube surfaces from the exhaustive load-pulls are spaced in such a way that the resolution around the optimum location is larger than that of the algorithm-based search's step size. This illustrates that excellent resolution can be obtained by the quick search even if there is no initial information known about the optimum.

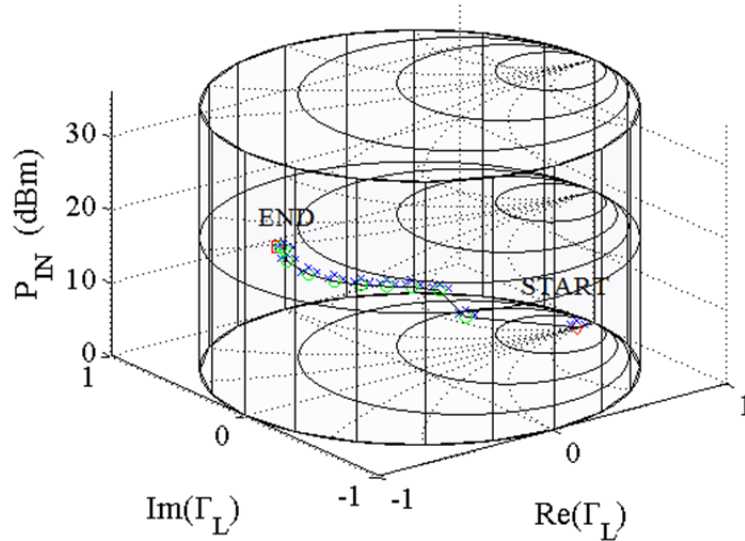


Figure 3.4: Simulated search algorithm trajectory through the Power Smith Tube with parameters;  $D_s = 1$ , input power range  $0 \text{ dBm} \leq P_{in} \leq 36 \text{ dBm}$  and a starting location  $\Gamma_L = 0.90\angle 0^\circ$ ,  $P_{in} = 0 \text{ dBm}$ . The search required 42 measured points and converged to the endpoint  $\Gamma_L = 0.77\angle 176.4^\circ$  and  $P_{in} = 21.21 \text{ dBm}$ , where PAE = 41.44% and ACPR = -40.05 dBc.

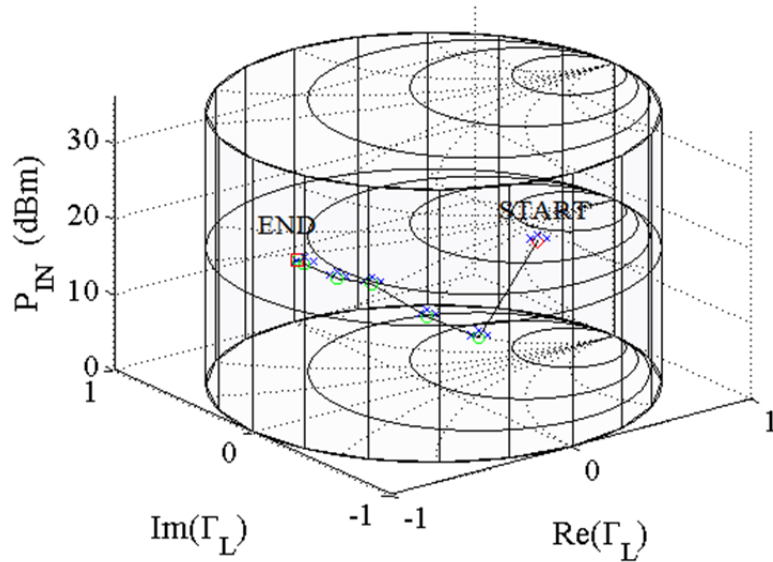


Figure 3.5: Simulated search algorithm trajectory through the Power Smith Tube with parameters;  $D_s = 1$ , input power range  $0 \text{ dBm} \leq P_{in} \leq 36 \text{ dBm}$  and a starting location  $\Gamma_L = 0.75 \angle -90^\circ$ ,  $P_{in} = 25 \text{ dBm}$ . The search required 26 measured points and converged to the endpoint  $\Gamma_L = 0.75 \angle -179.6^\circ$  and  $P_{in} = 21.07 \text{ dBm}$ , where PAE = 40.76% and ACPR = -40.15 dBc.

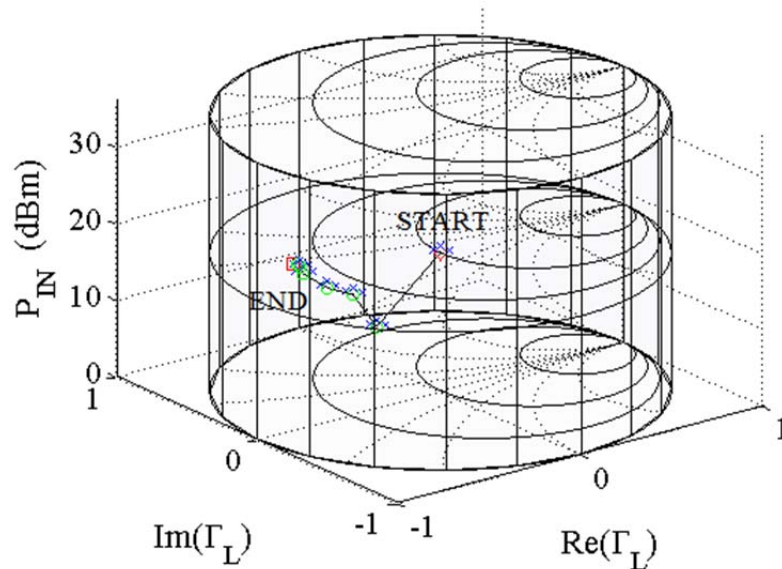


Figure 3.6: Simulated search algorithm trajectory through the Power Smith Tube with parameters;  $D_s = 1$ , input power range  $0 \text{ dBm} \leq P_{in} \leq 36 \text{ dBm}$  and a starting location  $\Gamma_L = 0 \angle 0^\circ$ ,  $P_{in} = 18 \text{ dBm}$ . The search required 28 measured points and converged to the endpoint  $\Gamma_L = 0.76 \angle 175.7^\circ$  and  $P_{in} = 20.89 \text{ dBm}$ , where PAE = 40.78% and ACPR = -40.14 dBc.

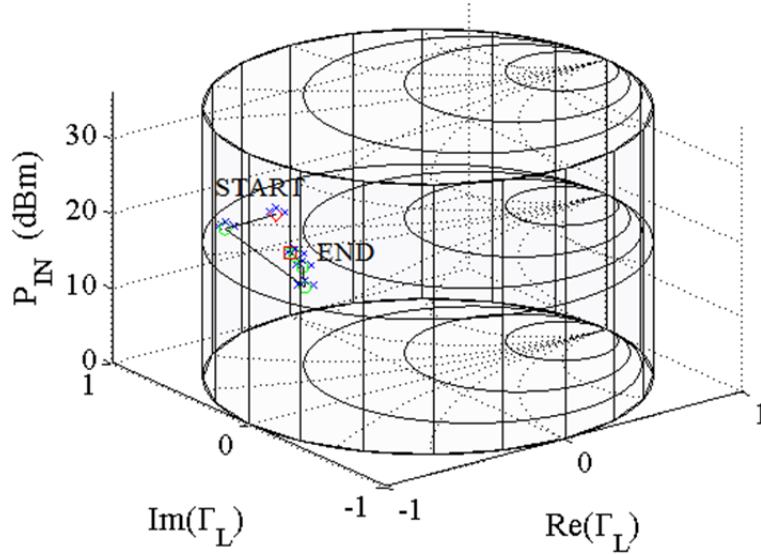


Figure 3.7: Simulated search algorithm trajectory through the Power Smith Tube with parameters;  $D_s = 1$ , input power range  $0 \text{ dBm} \leq P_{in} \leq 36 \text{ dBm}$  and a starting location  $\Gamma_L = 0.85 \angle 180^\circ$ ,  $P_{in} = 27 \text{ dBm}$ . The search required 25 measured points and converged to the endpoint  $\Gamma_L = 0.76 \angle 179.3^\circ$  and  $P_{in} = 21.23 \text{ dBm}$ , where PAE = 40.88% and ACPR = -40.18 dBc.

TABLE 3.1: SUMMARY OF SIMUALATION RESULTS

Start $\Gamma_L$	Start $P_{in}$ (dBm)	End $\Gamma_L$	End $P_{in}$ (dBm)	End ACPR (dBc)	End PAE (%)	# Ms.
$0.5 \angle 90^\circ$	5	$0.79 \angle -178^\circ$	21.59	-40.08	41.13	29
$0.9 \angle 0^\circ$	0	$0.77 \angle 176^\circ$	21.21	-40.05	41.44	42
$0.75 \angle -90^\circ$	25	$0.75 \angle -180^\circ$	21.07	-40.15	40.76	26
$0 \angle 0^\circ$	18	$0.76 \angle 176^\circ$	20.89	-40.14	40.78	28
$0.85 \angle 180^\circ$	27	$0.76 \angle 179^\circ$	21.23	-40.18	40.88	25

### 3.2.2 Measurement Results

The platform used to test the algorithm was the same as the bench setup depicted in Figure 2.10 in the previous chapter. For the measurement a SKY5017-70LF InGaP

packaged amplifier was biased and used as the device under test (DUT). Measurements of PAE were performed with a Keysight Technologies power meter and sensor, and a Keysight spectrum analyzer was used to measure ACPR. Because this device is different from the ADS built in PA used in the last section, the DUT should exhibit unrelated behavior. This allows algorithm performance to be evaluated for a different, unrelated device. All of the measurement tests of the algorithm were performed using a step size of  $D_s = 1$ , neighboring point distance of  $D_n = 0.05$ , and an input power range of  $-5 \text{ dBm} \leq P_{in} \leq 2 \text{ dBm}$ . Since the device used in this test measurement setup is inherently different than the previous amplifier, the ACPR limit was set to  $-27.5 \text{ dBc}$  for the search.

For the Skyworks packaged amplifier, the signal input power level maximum was chosen as  $2 \text{ dBm}$  based on information from the provided data sheet. Due to the nature of the search algorithm this power level was strictly imposed in order to prevent operation at locations with poor efficiency and high power levels, which could damage the PA. In order to effectively test the search algorithm through measurement it is important to select an ACPR limit that is neither too strict nor too lenient to obtain an acceptable region that allows for a challenging optimization. For example, if the ACPR limit is too strict the optimization becomes trivial because the resulting acceptable region is insignificant. On the contrary, if the ACPR limit is too lenient then nearly the entire Power Smith Tube becomes acceptable which would make the search algorithm an unconstrained optimization. The resulting ACPR surface for this device can be seen in the previous chapter in Figure 2.12.

Figures 3.8 through 3.12 illustrate the trajectory of the search algorithm for different starting combinations of  $\Gamma_L$  and  $P_{in}$ . The search results all show excellent

correspondence to each other, similarly to the previous simulations. The search results for measurement are summarized in Table 3.2. It can be seen that the variation of the endpoint for  $P_{in}$  across the five searches is less than 0.5 dB. The PAE found at the end locations for all five searches varies by less than 0.5 percent. All the ACPR values found at the endpoint are also beneath the limit and within 0.4 dB of the limiting ACPR value of -27.5 dBc. Also, the number of measurements ranges from 23 to 39 for all of the searches. The number of measurements required for the search to converge appears to be dependent on factors such as the search starting point location relative to the optimum point.

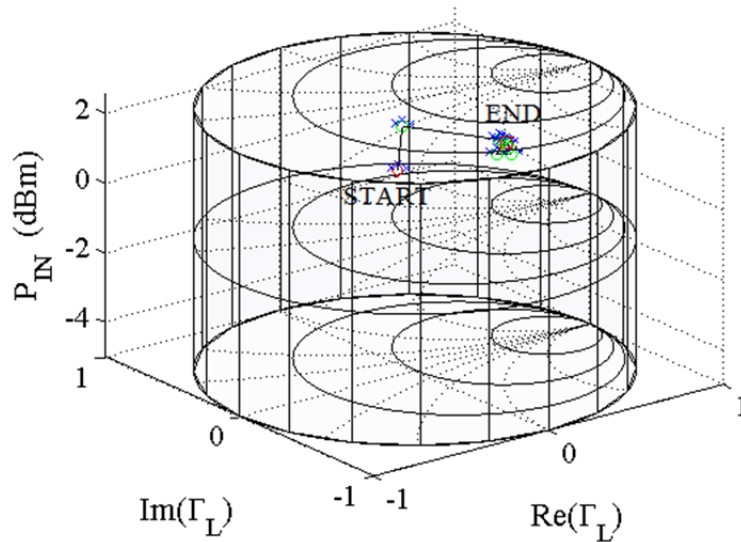


Figure 3.8: Search algorithm trajectory through the Power Tube performed in measurement with the parameters;  $D_s = 1$ ,  $D_n = 0.05$ , input power range  $-5 \text{ dBm} \leq P_{in} \leq 2 \text{ dBm}$ , and starting location  $\Gamma_L = 0.6 \angle -135^\circ$ ,  $P_{in} = 2 \text{ dBm}$ . The search required 31 measurement point and converged to the endpoint  $\Gamma_L = 0.42 \angle -44.32^\circ$  and  $P_{in} = 1.60 \text{ dBm}$ , where  $\text{PAE} = 7.32\%$  and  $\text{ACPR} = -27.55 \text{ dBc}$ .

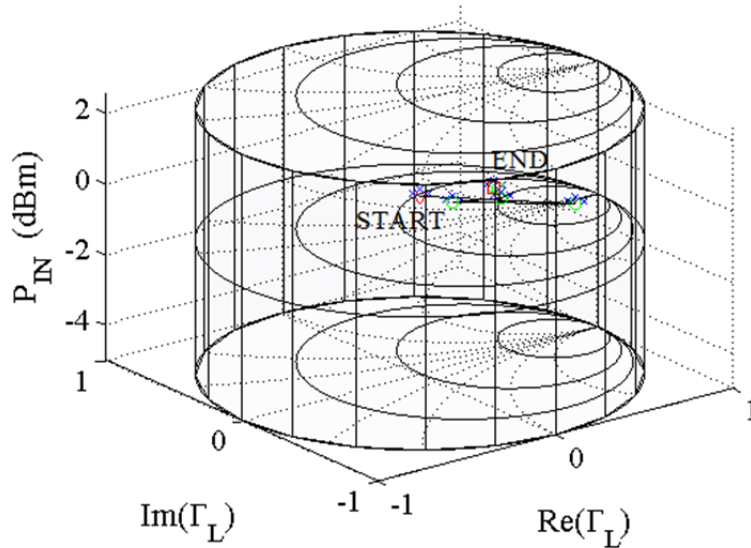


Figure 3.9: Search algorithm trajectory through the Power Tube performed in measurement with the parameters;  $D_s = 1$ ,  $D_n = 0.05$ , input power range  $-5 \text{ dBm} \leq P_{in} \leq 2 \text{ dBm}$ , and starting location  $\Gamma_L = 0 \angle 0^\circ$ ,  $P_{in} = 0 \text{ dBm}$ . The search required 19 measurement points and converged to the endpoint  $\Gamma_L = 0.45 \angle -46.61^\circ$  and  $P_{in} = 1.58 \text{ dBm}$ , where PAE = 7.05% and ACPR = -27.86 dBc.

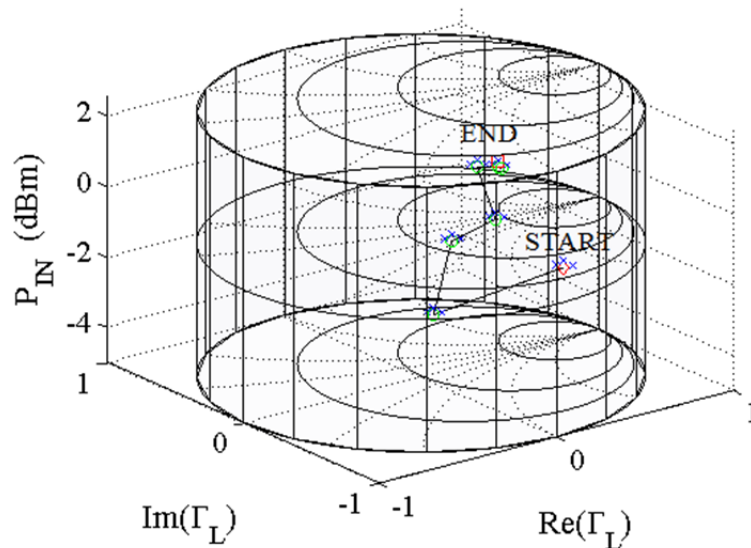


Figure 3.10: Search algorithm trajectory through the Power Tube performed in measurement with the parameters;  $D_s = 1$ ,  $D_n = 0.05$ , input power range  $-5 \text{ dBm} \leq P_{in} \leq 2 \text{ dBm}$ , and starting location  $\Gamma_L = 0.8 \angle 0^\circ$ ,  $P_{in} = -3 \text{ dBm}$ . The search required 35 measurement points and converged to the endpoint  $\Gamma_L = 0.43 \angle -24.12^\circ$  and  $P_{in} = 1.57 \text{ dBm}$ , where PAE = 7.49% and ACPR = -27.51 dBc.

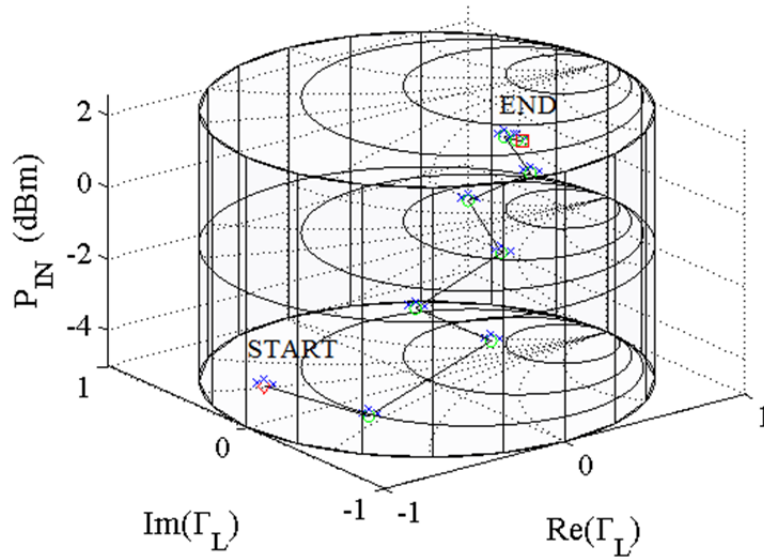


Figure 3.11: Search algorithm trajectory through the Power Tube performed in measurement with the parameters;  $D_s = 1$ ,  $D_n = 0.05$ , input power range  $-5 \text{ dBm} \leq P_{in} \leq 2 \text{ dBm}$ , and starting location  $\Gamma_L = 0.9 \angle 180^\circ$ ,  $P_{in} = -4 \text{ dBm}$ . The search required 39 measurement points and converged to the endpoint  $\Gamma_L = 0.42 \angle -40.33^\circ$  and  $P_{in} = 1.67 \text{ dBm}$ , where PAE = 7.23% and ACPR = -27.80 dBc.

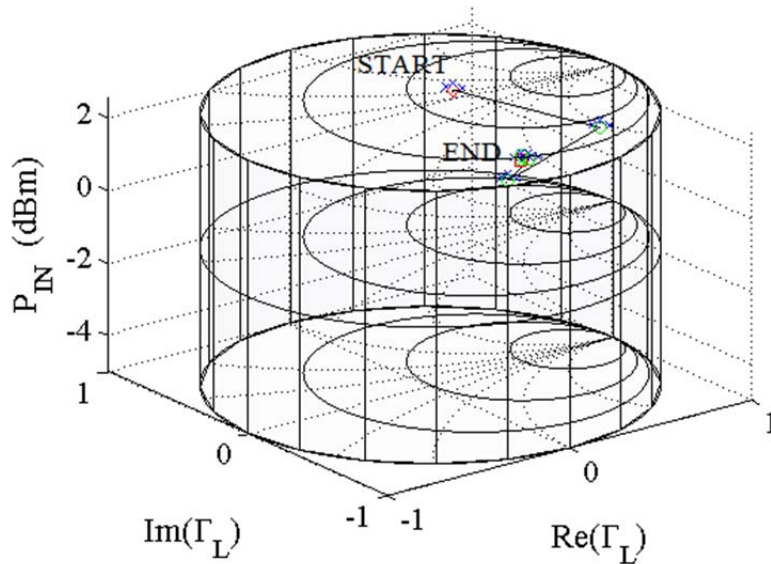


Figure 3.12: Search algorithm trajectory through the Power Tube performed in measurement with the parameters;  $D_s = 1$ ,  $D_n = 0.05$ , input power range  $-5 \text{ dBm} \leq P_{in} \leq 2 \text{ dBm}$ , and starting location  $\Gamma_L = 0.75 \angle 45^\circ$ ,  $P_{in} = 1.5 \text{ dBm}$ . The search required 24 measurement points and converged to the endpoint  $\Gamma_L = 0.39 \angle -38.37^\circ$  and  $P_{in} = 1.21 \text{ dBm}$ , where PAE = 7.29% and ACPR = -27.51 dBc.

TABLE 3.2: SUMMARY OF MEASUREMENT RESULTS

Start $\Gamma_L$	Start $P_{in}$ (dBm)	End $\Gamma_L$	End $P_{in}$ (dBm)	End ACPR (dBc)	End PAE (%)	# Ms.
$0.6\angle -135^\circ$	2.0	$0.42\angle -44^\circ$	1.60	-27.55	7.32	31
$0\angle 0^\circ$	0.0	$0.45\angle -47^\circ$	1.58	-27.86	7.05	23
$0.8\angle 0^\circ$	-3.0	$0.43\angle -24^\circ$	1.57	-27.51	7.49	35
$0.9\angle 180^\circ$	-4.0	$0.42\angle -40^\circ$	1.67	-27.80	7.23	39
$0.75\angle 45^\circ$	1.5	$0.39\angle -38^\circ$	1.21	-27.51	7.29	24

The results seen in Table 3.2 for the measurement DUT correspond well with the results seen in Table 3.1 for the simulation device. Both tables demonstrate the developed search algorithm's consistency in optimizing for multiple constraints. In both measurement and simulation, the search results taken at multiple starting points show consistent and accurate convergence when compared to the traditional iterative load-pull evaluations performed at multiple input power levels. Additionally, both measurement and simulation demonstrate the ability to improve the resolution of the optimum operating location when compared to traditional load-pull techniques. Due to the improved resolution, the search has the ability to obtain a higher power-added efficiency while still meeting ACPR requirements, all without having to perform dense load-pull measurements.

The proposed search algorithm decreases both time and skill required to optimize a power amplifier. The decrease in time and skill needed allows the algorithm to be applicable in a PA design environment, as well as in real-time reconfigurable amplifiers. This is demonstrated through the repeatability of the algorithm for multiple starting

points within the search space. Since the starting location of the search merely affects the number of measurements rather than the final operating location, the search can be run by a novice PA designer and the results would be comparable to that of a professional designer.

### 3.3 Momentum Aided Search

Reconfigurable power amplifiers facilitate cognitive radio transmissions by allowing reconfigurability for multiple frequency bands and operating conditions [44, 45] while also meeting spectral requirements, which may vary dynamically. A previously published paper presents an effective algorithm to find the optimum power added efficiency with a given adjacent channel power ratio [20]. This previously presented search has been modified to include the use of momentum, which has been shown to improve algorithm speed and effectiveness [46, 47, 48].

Adding momentum in to the previous gradient-based search allows preceding candidate points to influence the selection of subsequent candidate points. The momentum-adjusted search vector,  $\bar{w}_{k+1}$ , for the  $(k + 1)th$  point based on the adjusted search vector,  $\bar{w}_k$ , at the  $kth$  point and the search vector,  $\bar{v}_{k+1}$ , calculated for the  $(k + 1)th$  point is given as follows:

$$\bar{w}_{k+1} = \alpha \bar{w}_k + (1 - \alpha) \bar{v}_{k+1} \quad (3.11)$$

In the above equation,  $\alpha$  represents the momentum coefficient, which is assigned a value between 0 and 1. When  $\alpha$  is increased, more momentum is included in the search, and when  $\alpha$  is decreased, less momentum is included in the search. The value of  $\alpha$  directly represents the ratio of  $\bar{w}_k$  (previous step) and  $\bar{v}_{k+1}$  (current calculated step) to be included in the current step. For the special case of  $\alpha = 0$ , the search contains no

momentum and  $\bar{w}_{k+1} = \bar{w}_k$ . For the opposite extreme case of  $\alpha = 1$ ,  $\bar{w}_{k+1} = \bar{w}_k$ , and the search vector never changes from the first step because it is always equal to its previous value.

It can be seen through equation 3.11 that when the calculated gradient continues to point in the same direction, the size of the search vector will increase as the search moves toward the constrained operating location. On the other hand, if the calculated gradient continues changing directions the momentum will straighten out the variations. Since the calculation of the search algorithms in reconfigurable power amplifiers will be based on real measurements which will contain noise, this will be particularly useful.

The momentum-aided algorithm was tested in measurement using the same equipment as in Figure 2.10 where the Skyworks SKY5017-70LF InGaP packaged amplifier was the DUT. Similarly to the gradient search algorithm, the goal of the search is to find the combination of  $\Gamma_L$  and input power  $P_{in}$  to provide the maximum PAE while maintaining an ACPR below the constraint value of -27.5 dBc. Because the search is designed for real time adaptive power amplifiers, the total measured points and the final PAE are the metrics of quality. The search trajectory for the starting point  $\Gamma_L = 0\angle 0^\circ$ ,  $P_{in} = -3$  dBm can be seen in Figures 3.13 through 3.15 below where  $\alpha$  is varied from 0 to 0.4.

In the figures below it can be seen that as the momentum is increased from 0, to 0.2, to 0.4 the search path becomes straighter. Not only does the search appear to proceed more directly toward the endpoint, but also the number of measured points decreases and the end PAE increases. For these particular parameters the addition of momentum increases both the accuracy and speed of the search.

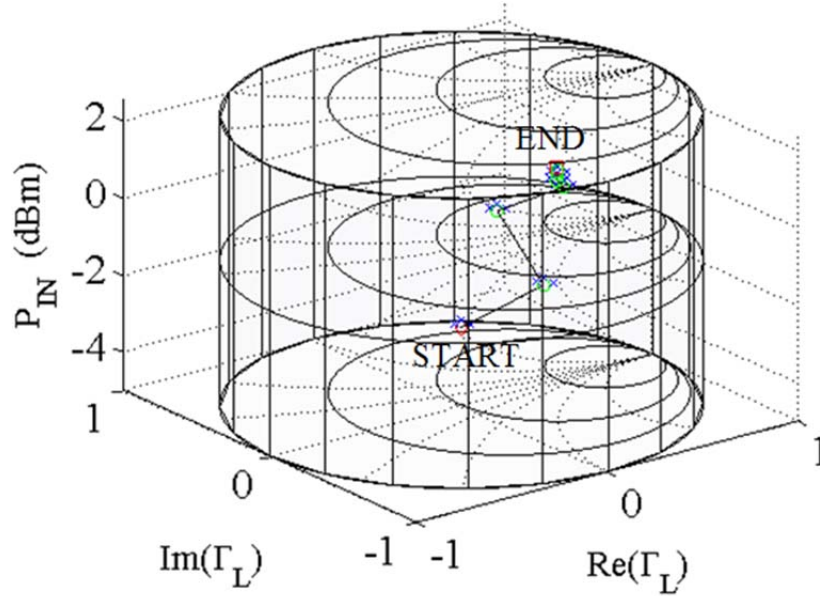


Figure 3.13: Momentum-aided search algorithm trajectory through the Power Smith Tube at the starting location of  $\Gamma_L = 0 \angle 0^\circ$ ,  $P_{in} = -3 \text{ dBm}$ . A momentum value of 0 was used for this search and the optimum location found after 28 measurements was  $\Gamma_L = 0.40 \angle -28.6^\circ$  at  $P_{in} = 1.03 \text{ dBm}$  with PAE = 7.01% and ACPR = -28.06 dBc.

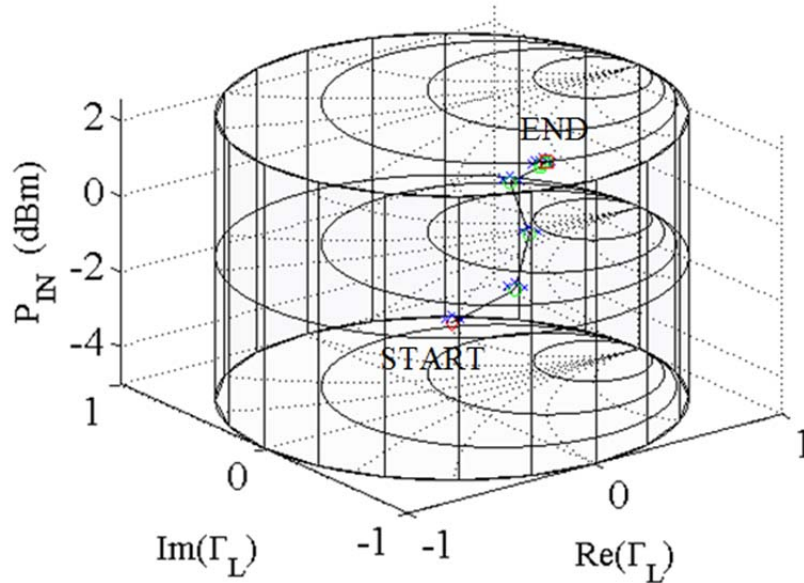


Figure 3.14: Momentum-aided search algorithm trajectory through the Power Smith Tube at the starting location of  $\Gamma_L = 0 \angle 0^\circ$ ,  $P_{in} = -3 \text{ dBm}$ . A momentum value of 0.2 was used for this search and the optimum location found after 26 measurements was  $\Gamma_L = 0.40 \angle -46.0^\circ$  at  $P_{in} = 1.38 \text{ dBm}$  with PAE = 7.37% and ACPR = -27.55 dBc.

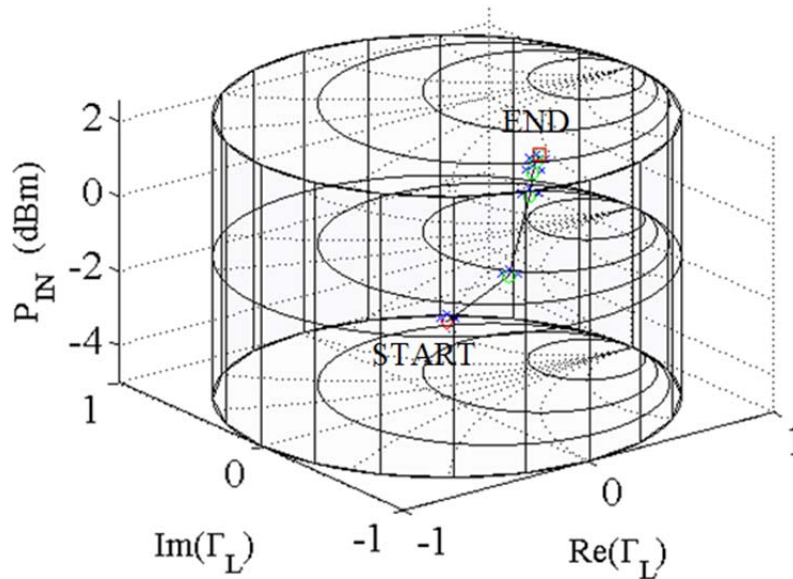


Figure 3.15: Momentum-aided search algorithm trajectory through the Power Smith Tube at the starting location of  $\Gamma_L = 0 \angle 0^\circ$ ,  $P_{in} = -3 \text{ dBm}$ . A momentum value of 0.4 was used for this search and the optimum location found after 24 measurements was  $\Gamma_L = 0.40 \angle -32.6^\circ$  at  $P_{in} = 1.39 \text{ dBm}$  with  $\text{PAE} = 7.45\%$  and  $\text{ACPR} = -27.62 \text{ dBc}$ .

However, increasing the momentum will not always improve a search's performance. The effect momentum has on a search depends upon several factors. For example, if the starting location is near the optimum operating location, adding a significant amount of momentum may hinder a search's performance. This is because the gradients around the optimum are steep and vary greatly depending on location in relation to the optimum. On the contrary, if the search's starting location is far from the optimum operating location then more momentum will benefit the search. This is due to the effect measurement noise has on the gradient calculations taken. Another example of the increased momentum in a search can be seen in Figures 3.16 to 3.18, where the axes are flipped to better illustrate the search trajectory.

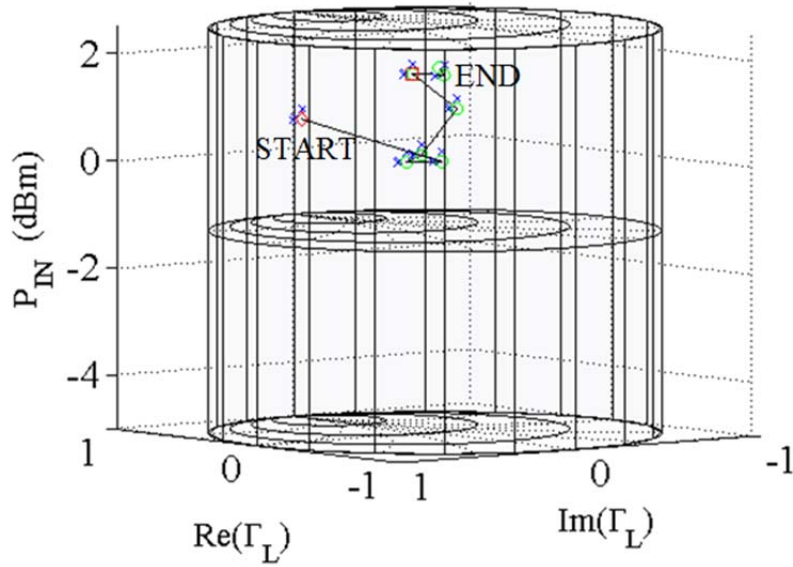


Figure 3.16: Momentum-aided search algorithm trajectory through the Power Smith Tube at the starting location of  $\Gamma_L = 0.75 \angle 90^\circ$ ,  $P_{in} = 1 \text{ dBm}$ . A momentum value of 0 was used for this search and the optimum location found after 31 measurements was  $\Gamma_L = 0.39 \angle -26.9^\circ$  at  $P_{in} = 1.50 \text{ dBm}$  with PAE = 7.37% and ACPR = -27.78 dBc.

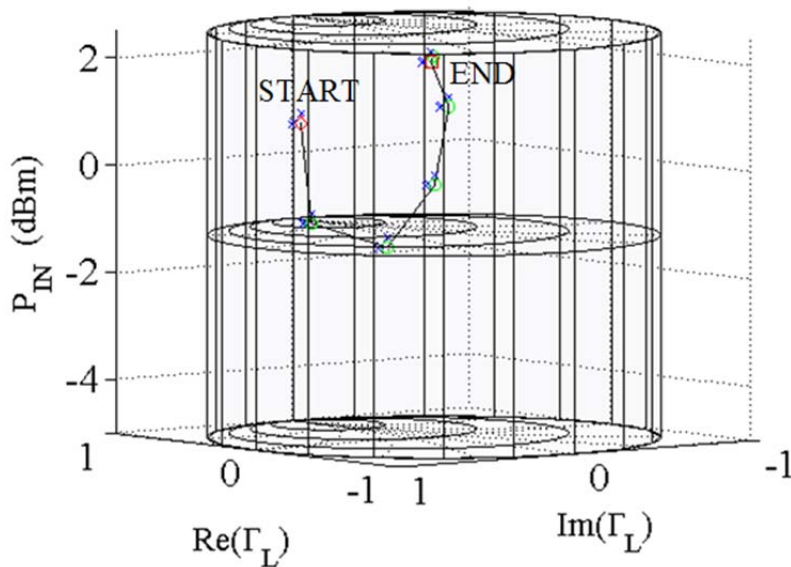


Figure 3.17: Momentum-aided search algorithm trajectory through the Power Smith Tube at the starting location of  $\Gamma_L = 0.75 \angle 90^\circ$ ,  $P_{in} = 1 \text{ dBm}$ . A momentum value of 0.2 was used for this search and the optimum location found after 26 measurements was  $\Gamma_L = 0.42 \angle -36.7^\circ$  at  $P_{in} = 1.79 \text{ dBm}$  with PAE = 7.64% and ACPR = -27.60 dBc.

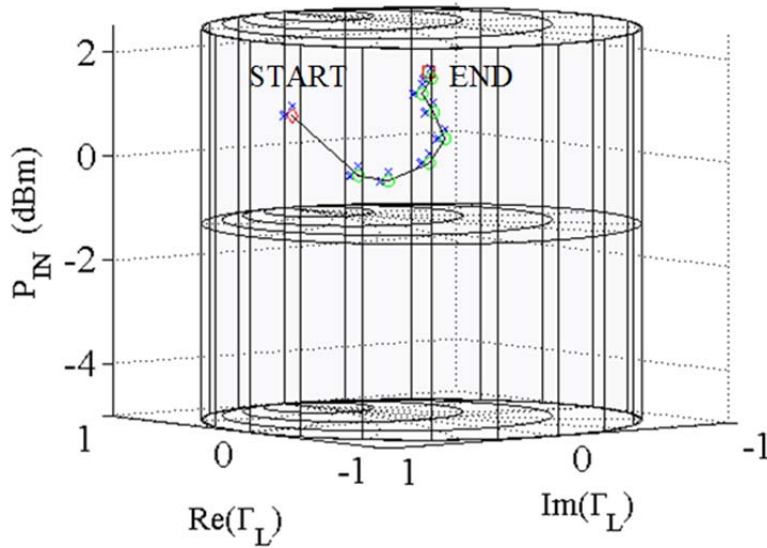


Figure 3.18: Momentum-aided search algorithm trajectory through the Power Smith Tube at the starting location of  $\Gamma_L = 0.75 \angle 90^\circ$ ,  $P_{in} = 1 \text{ dBm}$ . A momentum value of 0.4 was used for this search and the optimum location found after 34 measurements was  $\Gamma_L = 0.43 \angle -43.0^\circ$  at  $P_{in} = 1.49 \text{ dBm}$  with PAE = 7.58% and ACPR = -27.70 dBc.

Figures 3.16 through 3.18 illustrate the negative impact too much momentum can have upon a search. It is important to note that in Figures 3.16 through 3.18 the x and y axes are interchanged when compared to Figures 3.13 through 3.15. This is because it is easier to see the trajectory through the Power Tube at this angle. In Figure 3.16 the momentum coefficient is set to  $\alpha = 0$ , and as a direct result the search moves back and forth to the optimum operating location. This back-and-forth effect can be attributed to the change in the search's direction vector after the first step. Since the search's starting point is outside of ACPR compliance, the first step is taken in the direction of the ACPR vector found in equation 3.2. This step in the ACPR gradient direction led the search to jump towards the interior of the ACPR acceptable region for the next candidate. Because the next candidate is inside the ACPR region, the PAE gradient vector is included in the subsequent step, which can be seen in equation 3.10.

In Figure 3.17 a momentum coefficient of  $\alpha = 0.2$  is used, and as a result the search trajectory takes a smoother approach toward the optimum location. It can also be noted that this search has an initial downward step for the same reason as the search containing no momentum. This initial downward step remains in the search for the next few consecutive steps with its impact decaying as more steps are taken. Even with the initial step factored into subsequent steps, the reduced back-and-forth motion or influence of noise aids the search in both obtaining a higher PAE and finding the optimum in fewer measurements. Since the momentum coefficient in the search shown in Figure 3.18 is  $\alpha = 0.4$ , the initial downward step has more impact on the search's future steps. Though this search is smoother visually than the previous two from the same starting location, the search performs more poorly and requires more measurements. This conceptually makes sense because larger amounts of momentum inhibit a search's sensitivity to surrounding calculated neighboring gradients by reducing the contribution these gradients have on the search's next candidate.

Table 3.3 shows the results for different momentum levels from multiple starting points throughout the Power Smith Tube. Similarly to previous examples, each search was implemented on a Skyworks SKY5017-70LF InGaP packaged amplifier. It can be noted in the table that in most cases, adding a moderate level of momentum tends to make the resulting PAE higher and the ACPR closer to its limit. Additionally, momentum can be seen to generally decrease the number of measurements for searches further away from the ideal operating location.

TABLE 3.3: SUMMARY OF MOMENTUM RESULTS

Start $\Gamma_L, P_{in}$	$\alpha$	End $\Gamma_L$	End $P_{in}$ , dBm	End ACPR, dBc	End PAE %	# Ms
$0 \angle 0^\circ$  $P_{in} = -3$	0.0	$0.40 \angle -28.6^\circ$	1.03	-28.06	7.01	28
	0.1	$0.42 \angle -30.7^\circ$	1.61	-27.56	7.59	22
	0.2	$0.40 \angle -46.0^\circ$	1.38	-27.55	7.37	26
	0.3	$0.41 \angle -46.8^\circ$	1.45	-27.53	7.42	23
	0.4	$0.40 \angle -32.6^\circ$	1.39	-27.62	7.45	24
$0.8 \angle -175^\circ$  $P_{in} = -2$	0.0	$0.39 \angle -44.1^\circ$	1.27	-27.70	7.29	30
	0.1	$0.46 \angle -36.8^\circ$	1.72	-27.67	7.54	33
	0.2	$0.44 \angle -34.2^\circ$	1.81	-27.56	7.73	33
	0.3	$0.42 \angle -28.7^\circ$	1.76	-27.53	7.77	36
	0.4	$0.43 \angle -33.8^\circ$	1.60	-27.51	7.64	38
$0.25 \angle 45^\circ$  $P_{in} = 0$	0.0	$0.36 \angle -47.3^\circ$	1.06	-27.58	7.10	40
	0.1	$0.49 \angle -35.2^\circ$	1.87	-27.67	7.61	40
	0.2	$0.45 \angle -30.5^\circ$	1.86	-27.56	7.73	27
	0.3	$0.45 \angle -40.2^\circ$	1.78	-27.52	7.68	30
	0.4	$0.37 \angle -33.2^\circ$	1.22	-27.79	7.35	33
$0.5 \angle 135^\circ$  $P_{in} = 2$	0.0	$0.45 \angle -36.2^\circ$	1.34	-28.31	7.01	34
	0.1	$0.45 \angle -30.4^\circ$	1.95	-27.66	7.62	26
	0.2	$0.42 \angle -45.2^\circ$	1.63	-27.64	7.42	34
	0.3	$0.43 \angle -43.8^\circ$	1.64	-27.62	7.45	30
	0.4	$0.44 \angle -37.4^\circ$	1.65	-27.64	7.68	50
$0.75 \angle 90^\circ$  $P_{in} = 1$	0.0	$0.39 \angle -26.9^\circ$	1.50	-27.78	7.37	31
	0.1	$0.42 \angle -31.6^\circ$	1.87	-27.51	7.65	30
	0.2	$0.42 \angle -36.7^\circ$	1.79	-27.60	7.64	26
	0.3	$0.45 \angle -32.8^\circ$	2.07	-27.52	7.78	42
	0.4	$0.43 \angle -43.0^\circ$	1.49	-27.70	7.58	34
$0.4 \angle -90^\circ$  $P_{in} = -1$	0.0	$0.35 \angle -36.7^\circ$	1.16	-27.72	7.10	25
	0.1	$0.44 \angle -41.3^\circ$	1.81	-27.59	7.66	28
	0.2	$0.39 \angle -37.6^\circ$	1.52	-27.64	7.46	19
	0.3	$0.42 \angle -36.0^\circ$	1.63	-27.51	7.57	19
	0.4	$0.40 \angle -24.2^\circ$	1.55	-27.62	7.56	20

For some of the starting points in Table 3.3, a momentum coefficient of  $\alpha = 0.4$  is too large and often results in less desirable results with lower PAE and more measurements. A large amount of momentum can decrease a search's sensitivity to steep gradients around a constrained optimum operating location and is therefore discouraged. However, a smaller amount of momentum is shown to minimize the effect noise, or the impact a faulty measurement has on a search's progression through the Power Smith Tube. In most cases a momentum coefficient of  $\alpha = 0.2$  or  $0.3$  proves to be effective in increasing a search's performance.

With appropriate momentum, the trajectory of the search in the Power Smith Tube is observed to straighten and become less sensitive to measurement-based gradient calculation noise. For real time adaptive radar and communication systems an increased robustness in noisy environments is important. Momentum included in an optimization search shows promise for decreasing circuit reconfiguration time and increasing optimization accuracy for cognitive and reconfigurable radio applications.

### *3.4 Summary*

A fast search algorithm has been presented and supported for the purpose of the simultaneous optimization of power amplifier load-reflection coefficient and input-power to achieve maximum power-added efficiency while meeting the adjacent-channel power ratio requirements. This proposed search has demonstrated its effectiveness in obtaining high efficiency while also satisfying linearity requirements consistently in both measurement and simulation. Not only is high PAE achieved, but the number of measurements required to locate the constrained optimum is remarkably lower than the

number of measurements required for a load-pull based optimization technique. Excellent repeatability of the algorithm has been demonstrated in both measurement and simulation results from multiple starting locations. Additionally, a momentum-aided search has been proven to reduce the impact measurement-based noise has on wireless systems by increasing robustness.

## CHAPTER FOUR

### Optimization in Higher Dimensions

For real-time power amplifier reconfiguration, multiple factors must be considered simultaneously in order to achieve an optimal solution. Among these considerations are input power, load impedance, and bias voltages, which have been shown to directly influence power amplifier design performance [32]. A typical power amplifier optimization procedure involves tuning each of these parameters individually. This, in turn, requires numerous measurements to create load-pulls, power-sweeps and device current-voltage (IV) curves in both simulation and measurement. These measurements not only require design proficiency but also necessitate significant time and resources, and a constrained optimum solution is not guaranteed to be obtained. The aim of this chapter is to present multi-dimensional Smith Tubes as a means to visualize the dynamic power amplifier search space in higher N-dimensions. Furthermore, visualization for higher dimensions allows optimization of multiple parameters to be quickly conceptualized, which considerably simplifies both real-time optimization and power amplifier design. Section 4.1 discusses why optimization in a higher-dimensional search space is desirable. Section 4.2 proposes a method of visualization in higher dimensions, where Sections 4.2.1 and 4.2.2 examine four and five-dimensional visualizations, respectively. Section 4.3 then demonstrates a fast optimization method in higher dimensions, and finally Section 4.4 summarizes the presented results.

#### *4.1 Motivation for Higher Dimensional Optimization*

Typical power amplifier design involves an iterative approach of optimizing one parameter at a time. In order for suitable biasing conditions to be selected, current-voltage (IV) curves are created through device measurement on an oscilloscope or through software simulation. Because the created IV curves display the relationship between DC current through a device and DC voltage across its terminals, designers can determine the basic parameters of the DUT and model its behavior. The IV curve illustrates the relationship of a device's drain-to-source voltage  $V_{DS}$ , to its gate-to-source voltage,  $V_{GS}$ . After an appropriate biasing condition is selected, a power-sweep is performed to find a suitable  $P_{in}$  for signal operation. Finally, at the preferred  $P_{in}$ ,  $V_{DS}$ , and  $V_{GS}$  combination, a load-pull is performed and the corresponding  $\Gamma_L$  possessing the most desirable conditions is chosen. This three-step process is performed in a continuous loop since changing any single input parameter alters the constructed sweep, load-pull, or IV curve previously created. The single consideration loop ends when the designer is finally satisfied with the power amplifier results. This iterative process quickly becomes very time-consuming, as many measurements are needed to construct each graph.

The Power Smith Tube presented in Chapter Three proved useful for simultaneous consideration of both  $P_{in}$  and  $\Gamma_L$ . Therefore, it follows that a higher dimensional optimization can consequentially be simplified through a means of visualization. The need for an optimization solution has been presented in previous literature, where Weiss demonstrates a simultaneous optimization of both drain voltage and RF input power for efficiency [11]. The use of an adaptive gate bias control has been presented as a method to optimize the tradeoff of linearity and efficiency through an

envelope tracking technique [49]. Raab and Yang demonstrate the dependence of PAE on both load impedance and biasing conditions [50, 51]. A multidimensional Smith Tube is proposed in this chapter in order to simultaneously consider all of these design parameters. Once characterized, this multidimensional space can be quickly optimized through an intelligent search algorithm for simulation, measurement, and real time applications.

## *4.2 Visualization in Higher Dimensions*

### *4.2.1 Four-Dimensional Visualization*

In order to view four dimensions, a row of three-dimensional Power Smith Tubes can be aligned along an axis representing a fourth parameter. This idea of creating a higher-dimensional figure with multiple lower-dimensional figures is done in previous work in the form of a grid diagram [52] and a star diagram [53]. Fiener even refers to this type of visualization as a “world within worlds” [54]. A popular example of a higher-dimensional representation has been shown through the interpretation of Fisher’s Iris flower data [55] where multiple two-dimensional scatter plots are organized to demonstrate a four-dimensional space.

For a realistic optimization example, a Modelithics Microwave Technology MWT-1 GaAs MESFET was used as the device under test in ADS simulation. The use of a measurement-based model is helpful in simulation testing for higher-dimensions, because the simulated amplifier’s behavior in a certain range of the parameters has been validated with measured data. This is dissimilar to some built-in software models, which simply use default parameters that may or may not represent realistic nonlinear device

performance. For this particular device, the simulation model was matched to measurement load-pull and IV characteristic data for the following ranges:  $-10 \text{ dBm} \geq P_{in} \geq 15 \text{ dBm}$ ,  $0V \geq V_{DS} \geq 12V$ , and  $-2V \geq V_{GS} \geq 2V$ . In an effort to obtain results that correspond well to measurement data, simulations in this work are confined to this region. The simulated IV curves for the Modelithics MWT-1 GaAs MESFET model are shown in Figure 4.1.

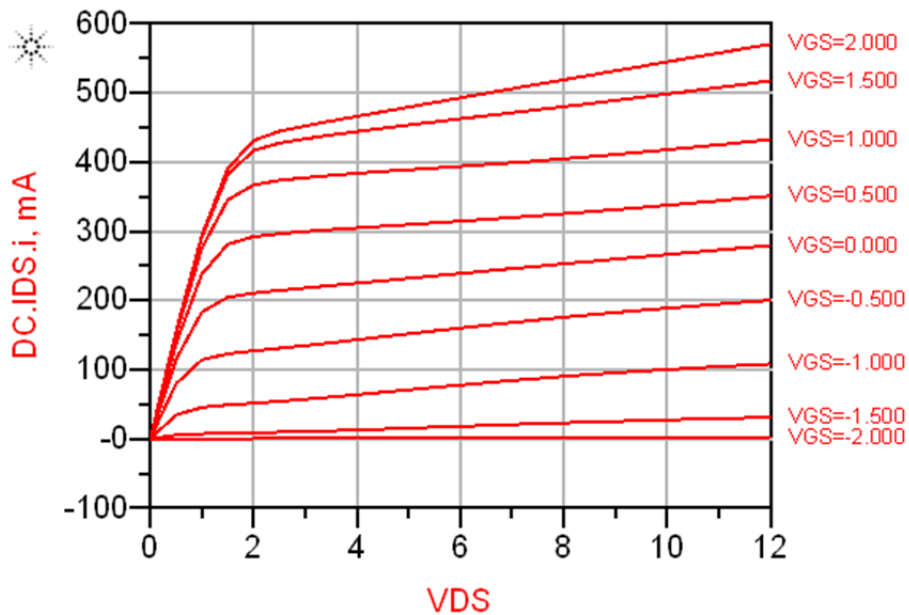


Figure 4.1: IV curves for Modelithics MWT-1 GaAs MESFET ADS model. To create this figure a  $V_{DS}$  and  $V_{GS}$  sweep was performed from  $0V$  to  $12V$  and  $-2V$  to  $2V$  respectively.

From the IV curves shown in Figure 4.1, appropriate  $V_{DS}$  values can be chosen for a four-dimensional grid diagram. By sliding and sampling a three-dimensional figure horizontally across a page, a fourth dimension can be constructed. Since the horizontal axis represents the fourth dimension of the search space, each shift in direction will have a direct effect on the three-dimensional figure. The effect of varying this fourth parameter

becomes apparent as the three-dimensional figure transforms. Due to the physical limitations of the horizontal axis, not every discrete location on the axis has a corresponding figure. However, if enough figures populate the horizontal axis the variations inside the three-dimensional figures can be conceptually interpolated between discrete locations. In Figure 4.2 the four-dimensional representation of the Power Smith Tube can be seen. In this figure the effect varying the input parameters  $\Gamma_L$ ,  $P_{in}$ , and  $V_{DS}$  have on linearity can be grasped. By incrementing the  $V_{DS}$  voltage by  $2V$  it is now possible to view the effect varying  $V_{DS}$  has on the ACPR surface inside the Power Smith Tube.

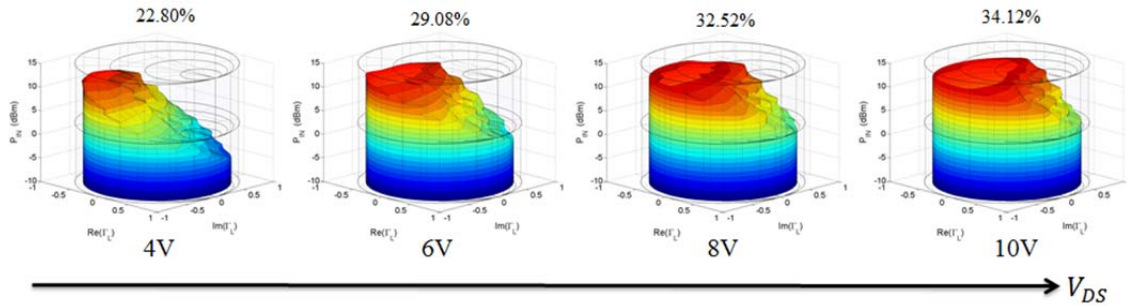


Figure 4.2: Grid view of a four-dimensional Power Smith Tube visualization with  $ACPR \leq -50$  dBc, and a  $V_{GS} = -0.5V$ . Each tube on  $V_{DS}$  axis represents a Power Smith Tube with a specified  $V_{DS}$  value of 4V, 6V, 8V, and 10V from left to right respectively. The optimum constrained design location for the combined tubes is found at:  $\Gamma_L = 0.15 \angle 105^\circ$ ,  $P_{in} = 13$  dBm,  $V_{DS} = 10$  V where  $PAE = 34.12\%$ . The highest PAE value found inside the acceptable ACPR surface for each  $V_{DS}$  value is shown above each Power Tube.

It can be noticed from Figure 4.2 that as  $V_{DS}$  is increased, the ACPR limiting surface increases in size, thus holding more possible operating points. This increase in linearity is expected since increasing  $V_{DS}$  changes the center of the load line on the IV plane: possibly to a trajectory that has more room to vary without bound. In such a

situation, the device can operate at higher levels of  $P_{in}$  before going into compression. For this device, the PAE contours originate towards the center of the Smith chart. Therefore, by increasing the acceptable operating region, locations closer to the center of the Smith chart become acceptable at higher levels of  $P_{in}$ . For this reason, the highest constrained PAE can be found at  $V_{DS} = 10V$  for Figure 4.2. This same experiment can be performed with the  $P_{in}$  and  $V_{DS}$  dimensions flipped. Flipping these dimensions would allow for a more continuous view of  $V_{DS}$  at the cost of not being able to view  $P_{in}$  continuously. For the sake of familiarity,  $P_{in}$  will remain the z-dimension while plotting higher dimensions in this chapter.

Not only does varying  $V_{DS}$  have an effect on the acceptable ACPR region,  $V_{DS}$  directly affects the efficiency of the power amplifier. Figure 4.3 below depicts the resulting surfaces for  $ACPR \leq -50$  dBc and  $PAE \geq 34.12\%$  in blue and red respectively. As expected, varying  $V_{DS}$  affects the PAE of the device at lower  $P_{in}$  levels. This is a result of how PAE is calculated, which can be seen in equation 2.1. Since  $V_{DS}$  represents DC biasing voltage for the power amplifier, increasing  $V_{DS}$  will negatively affect the PAE. However, it can be noted that there is an optimization tradeoff as seen in both Figure 4.2 and 4.3. Even though increasing  $V_{DS}$  decreases efficiency, the rate at which  $V_{DS}$  increases linearity is greater. As a result, a better operating location is found at a higher  $V_{DS}$ .

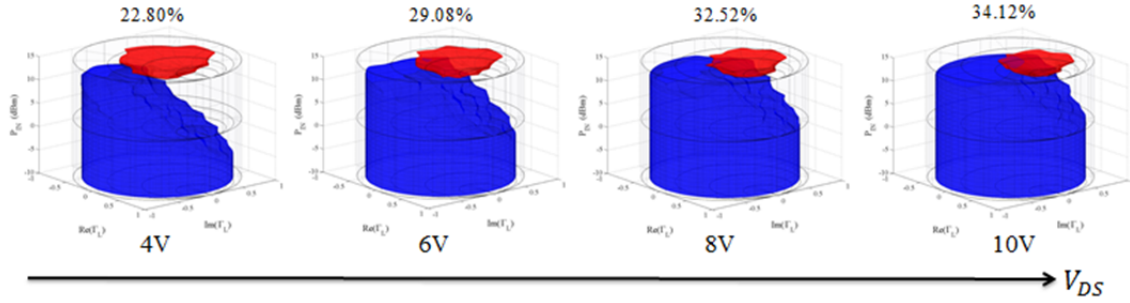


Figure 4.3: Grid view of a four-dimensional Power Smith Tube visualization with  $\text{ACPR} \leq -50 \text{ dBc}$  and  $V_{GS} = -0.5V$ . Each tube on  $V_{DS}$  axis represents a Power Tube with a specified  $V_{DS}$  value of 4V, 6V, 8V, and 10V from left to right respectively. The blue surface represents the  $\text{ACPR} \leq -50 \text{ dBc}$  surface and the red surface represents  $\text{PAE} \geq 34.12\%$ . The optimum constrained design location for the combined tubes is found at:  $\Gamma_L = 0.15 \angle 105^\circ$ ,  $P_{in} = 13 \text{ dBm}$ ,  $V_{DS} = 10 \text{ V}$  where  $\text{PAE} = 34.12\%$ . The highest PAE value found inside the acceptable ACPR surface for each  $V_{DS}$  value is shown above each Power Tube.

The difference between Figure 4.3 and Figure 4.4 is that the latter not only shows the  $\text{ACPR} \leq -50 \text{ dBc}$  surface, but also depicts the  $\text{PAE} \geq 34.12\%$  surface. By displaying both the ACPR and PAE surfaces simultaneously, the tradeoff between linearity and efficiency can be visualized. In the above figure, the  $\text{PAE} \geq 34.12\%$  surface intersects the ACPR surface only if there exists a constrained location with  $\text{ACPR} \leq -50 \text{ dBc}$  and  $\text{PAE} \geq 34.12\%$ . This intersection takes place at the  $V_{DS}$  values of 8V and 10V, but not at 4V and 6V. The gate-to-source voltage  $V_{GS}$  can be plotted in four-dimensions in a similar fashion. Figure 4.4 below depicts the four-dimensional representation of  $\Gamma_L$ ,  $P_{in}$ , and  $V_{GS}$  with  $V_{GS}$  displayed along the horizontal axis. Every Power Tube along this axis represents a different  $V_{GS}$  value and its corresponding  $\text{ACPR} \leq -50 \text{ dBc}$  surface.

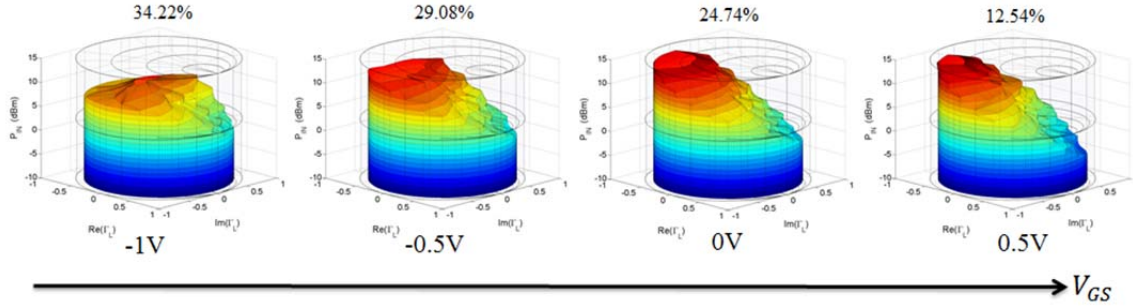


Figure 4.4: Grid view of a four-dimensional Power Smith Tube visualization with  $ACPR \leq -50$  dBc and  $V_{DS} = 6V$ . Each tube on the  $V_{GS}$  axis represents a Power Tube with a specified  $V_{GS}$  value of  $-1V$ ,  $-0.5V$ ,  $0V$ , and  $0.5V$  from left to right respectively. The optimum constrained design location for the combined tubes is found at:  $\Gamma_L = 0.15 \angle 90^\circ$ ,  $P_{in} = 9$  dBm,  $V_{GS} = -1V$  where PAE = 34.22%. The highest PAE value found inside the acceptable ACPR surface for each  $V_{DS}$  value is shown above each Power Tube.

From Figure 4.4 the effect increasing  $V_{GS}$  has on the  $ACPR \leq -50$  dBc surface can be seen. When  $V_{GS}$  is increased the ACPR surface shifts higher in the  $P_{in}$  dimension while also moving in the  $\Gamma_L$  dimension toward the left open circuit region of the Smith chart. The constrained optimum PAE seen above each Power Tube as a percentage tends to decrease as  $V_{GS}$  increases. The tradeoff of decreased linearity and increased efficiency is also visible in the previous four-dimensional  $V_{DS}$  grid. Here, however, decreasing  $V_{GS}$  results in an increase in the constrained optimum PAE, whereas previously an increase in  $V_{DS}$  resulted in an increase in the constrained optimum PAE.

The effect varying  $V_{GS}$  has on linearity and efficiency can be seen in Figure 4.5 below where the blue surface represents  $ACPR \geq -50$  dBc and the red surface represents  $PAE \geq 34.22\%$ . As  $V_{GS}$  increases, the  $PAE \geq 34.22\%$  surface quickly diminishes. It can also be noted that not only does the ACPR surface move in both the  $\Gamma_L$  and  $P_{in}$  dimensions, but the  $PAE \geq 34.22\%$  surface appears to move from the right closed circuit region of the Smith chart toward the center as  $V_{GS}$  is increased.

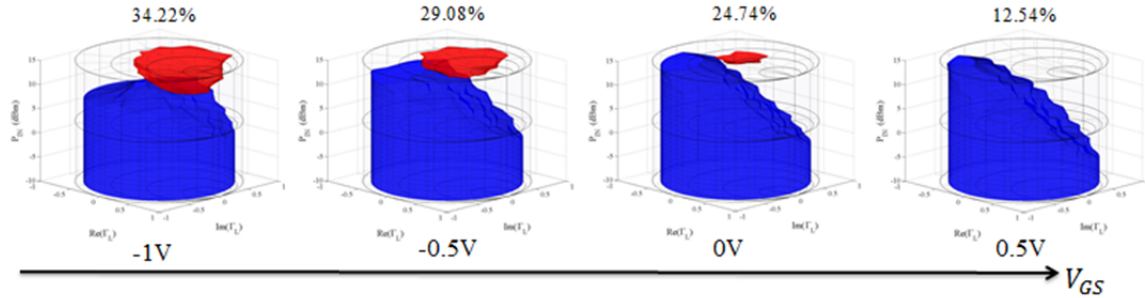


Figure 4.5: Grid view of a four-dimensional Power Smith Tube visualization with  $\text{ACPR} \leq -50 \text{ dBc}$ , and a  $V_{DS} = 6V$ . Each tube on  $V_{GS}$  axis represents a Power Tube with a specified  $V_{GS}$  value of  $-1V$ ,  $-0.5V$ ,  $0V$ , and  $0.5V$  from left to right respectively. The blue surface represents the  $\text{ACPR} \leq -50 \text{ dBc}$  surface and the red surface represents  $\text{PAE} \geq 34.22\%$ . The optimum constrained design location for the combined tubes is found at:  $\Gamma_L = 0.15 \angle 90^\circ$ ,  $P_{in} = 9 \text{ dBm}$ ,  $V_{GS} = -1V$  where  $\text{PAE} = 34.22\%$ .

#### 4.2.2. Five-Dimensional Visualization

The grid representation of four dimensions used in the previous section can be extrapolated into even higher dimensions. A fifth dimension can be added to the grid plotting method through the use of a vertical axis. This vertical axis can be used in conjunction with the previous horizontal axis in order to allow visualization of both  $V_{DS}$  and  $V_{GS}$  simultaneously. Since both  $V_{DS}$  and  $V_{GS}$  have been shown to directly affect linearity and efficiency [11] the resulting grid diagram will represent a dynamic five-dimensional space. For this experiment, the  $V_{DS}$  and  $V_{GS}$  dimensions will be depicted on the horizontal and vertical axes, respectively. This additional fifth dimension can be characterized as sliding a Power Tube down the page where each position represents a Power Tube with a different  $V_{GS}$  value. Due to the physical limitation of the page, the resulting change in  $V_{GS}$  will be discrete rather than continuous.

With the fourth and fifth dimensions represented as horizontal and vertical axes, the resulting diagram will form a grid of multiple rows and columns representing Power

Smith Tubes at different values of  $V_{DS}$  and  $V_{GS}$ . This, in turn, will enable the visualization of the dynamic effect varying the biasing conditions has on both efficiency and linearity simultaneously. In the diagram, moving diagonally down and to the right will represent not only a change in  $V_{DS}$ , but a change in  $V_{GS}$  as well. By viewing five total parameters at once, the optimization search space can be constructed and corresponding observations can be made.

For this example, the same Modelithics Microwave Technology MWT-1 GaAs MESFET device used to generate Figures 4.2 through 4.5 will be used. However, the difference here is that neither  $V_{GS}$  or  $V_{DS}$  will be held constant while the effects on the other are visualized. The resulting grid can be seen in Figure 4.6, where load-pulls were performed at  $P_{in}$  levels -10 dBm through 15 dBm at 1 dBm increments for each Power Tube. These Power Tubes were created at the  $V_{DS}$  levels of 4V through 10V at 2V increments. Finally, the  $V_{DS}$  rows were varied in  $V_{GS}$  from -1V to 0.5V with 0.5V increments. In total, 175 measurements were performed at 25 power levels for 16 total tubes, resulting in a grand total of 70,000 measurements required to create the five-dimensional grid seen in Figure 4.6 below.

It can be noticed from Figure 4.6 that at every level of  $V_{DS}$ , decreasing  $V_{GS}$  effectively decreases the acceptable ACPR region. Similarly, when  $V_{GS}$  is decreased for any given value of  $V_{DS}$ , the maximum constrained PAE value increases. This corresponds well with widely understood amplifier classifications, as increasing  $V_{GS}$  moves the amplifier into the linear region on the IV curve where behavior similar to a class A bias is exhibited. Class A biasing provides very low distortion, but is relatively inefficient. Consequently, when  $V_{GS}$  is decreased, the amplifier behaves more efficiently as the

quiescent operating point is shifted into the saturation region toward a class B biasing. It then follows that the resulting PAE is an improvement as a class B behavior is resultantly more efficient. As seen in four dimensions, increasing the  $V_{DS}$  voltage at any given  $V_{GS}$  value increases the constrained PAE due to the increased room for travel along an optimized load line.

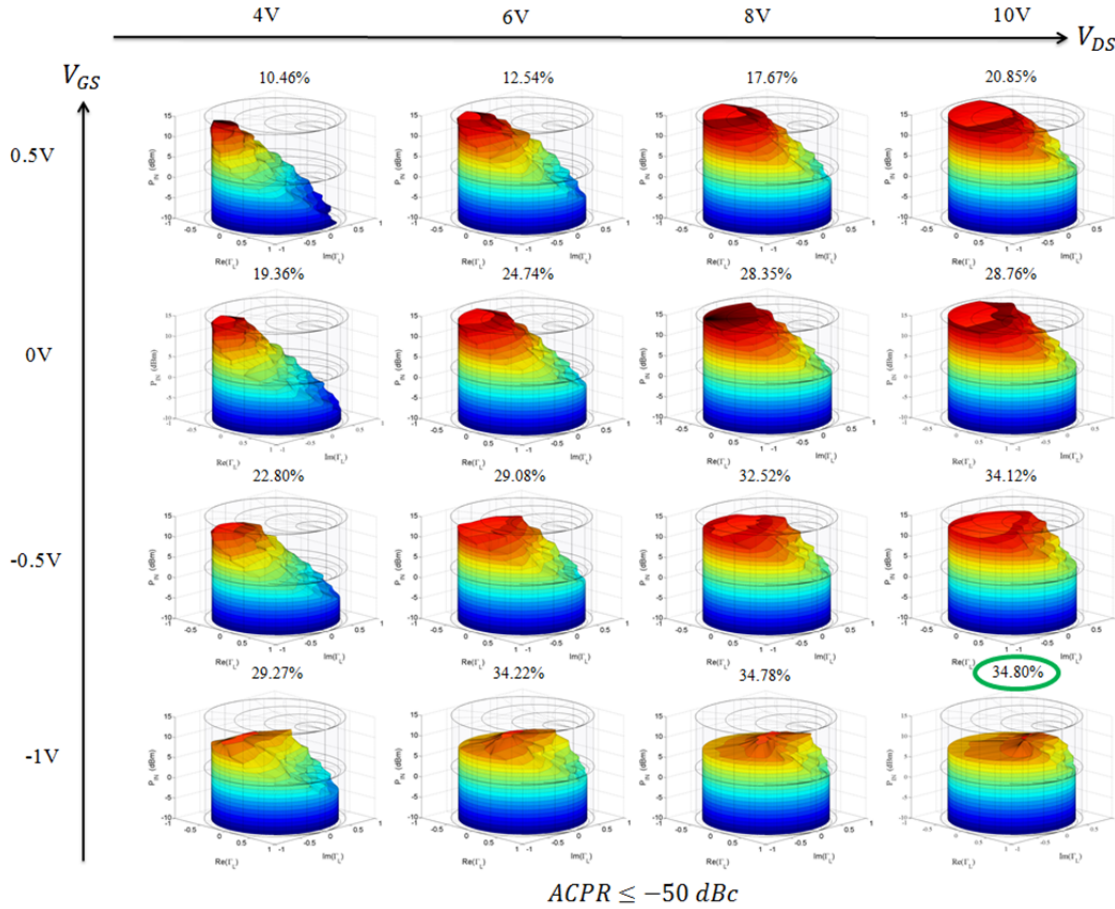


Figure 4.6: Five dimensional grid view of the Power Smith Tube with  $ACPR \leq -50 \text{ dBc}$ . Each tube on  $V_{DS}$  axis represents a Power Tube with a specified  $V_{DS}$  value of 4V, 6V, 8V, and 10V from left to right respectively. Each Tube on the  $V_{GS}$  axis represents a Power Tube with a specified  $V_{GS}$  value of 0.5V, 0V, 8V, 10V from top to bottom respectively. The optimum constrained design location for the combined tubes is found at:  $\Gamma_L = 0.30 \angle 60^\circ$ ,  $P_{in} = 10 \text{ dBm}$ ,  $V_{DS} = 10 \text{ V}$ , and  $V_{GS} = -1 \text{ V}$  where  $PAE = 34.80\%$ .

This five-dimensional diagram can also be created to visualize both PAE and ACPR surfaces simultaneously. The resulting grid can be seen below in Figure 4.7 where each Power Smith Tube corresponds to different combinations of  $V_{DS}$  and  $V_{GS}$ . The resulting PAE surface below exhibits similar characteristics to that seen in the previous section for the four-dimensional visualization. This PAE surface represents every PAE value  $\geq 34.80\%$  for the specified amplifier biasing conditions. As a result, the PAE surface only intersects the  $ACPR \leq -50$  dBc surface when the ACPR surface contains an operating point with a PAE of 34.80% or greater.

In Figure 4.7, the effect of varying the five parameters,  $Re(\Gamma_L)$ ,  $Im(\Gamma_L)$ ,  $P_{in}$ ,  $V_{DS}$ , and  $V_{GS}$  has on efficiency and linearity can be observed. For lower voltages of  $V_{DS}$  and constant  $V_{GS}$ , the resulting  $PAE \geq 34.80\%$  surface appears to grow in size. However, the linearity of the power amplifier decreases at a faster rate, which prevents both the surfaces from intersecting for different combinations of  $V_{DS}$  and  $V_{GS}$ . The Power Smith Tube with the highest constrained PAE can be seen in the bottom right of Figure 4.7 with  $V_{DS}$  and  $V_{GS}$  values of 10V and  $-1V$ , respectively. These biasing conditions produce the optimum operating location because, at this location, efficiency and linearity is maximized through the corresponding load line produced for IV characteristics. As expected, by moving diagonally from the bottom right to the top left of the five-dimensional diagram, the Power Tube possessing the worst PAE is exemplified. The poor efficiency seen in this particular Power Tube is a result of the biasing conditions as the associated quiescent point is near the device's knee region at low  $V_{DS}$ .

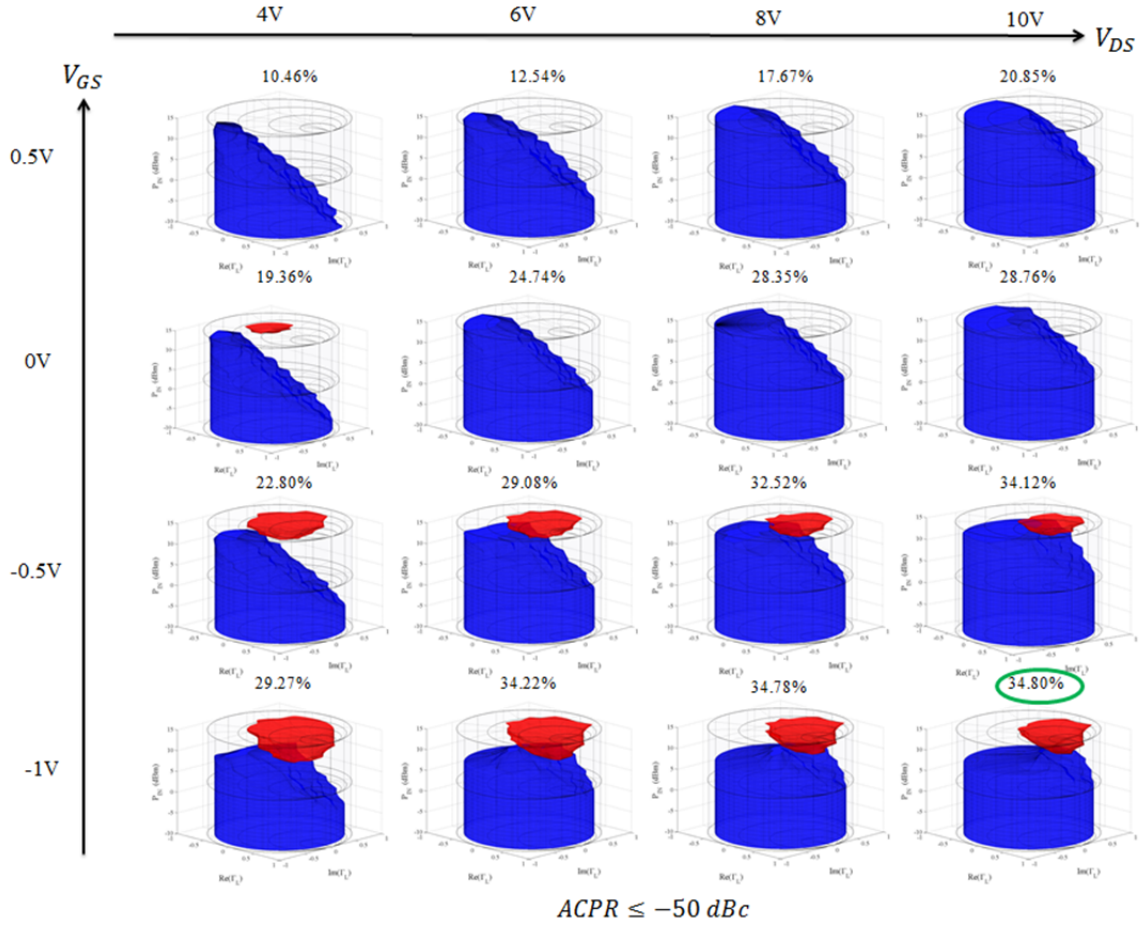


Figure 4.7: Five dimensional grid view of the Power Smith Tube with  $ACPR \leq -50$  dBc. Each tube on  $V_{DS}$  axis represents a Power Tube with a specified  $V_{DS}$  value of 4V, 6V, 8V, and 10V from left to right respectively. Each Tube on the  $V_{GS}$  axis represents a Power Tube with a specified  $V_{GS}$  value of 0.5V, 0V, 8V, 10V from top to bottom respectively. The blue surface for each plot represents the constrained  $ACPR \leq -50$  dBc surface, and the red surface represents the  $PAE \geq 34.80\%$  surface. The optimum constrained design location for the combined tubes is found at:  $\Gamma_L = 0.30 \angle 60^\circ$ ,  $P_{in} = 10$  dBm,  $V_{DS} = 10$  V, and  $V_{GS} = -1$  V where  $PAE = 34.80\%$ .

The five-dimensional characterization of the Modelithics model for the MWT-1 GaAs MESFET has proven to reduce the incumbent complexity of ACPR and PAE surfaces. All of the surfaces depicted in each Power Tube appear to possess Zadeh convexity [43]. However, the grid visualization of the five-dimensional space described

above lacks a continuous portrayal of  $V_{DS}$  and  $V_{GS}$ . As a result, the convexity of the depicted five-dimensional search space cannot be assumed with complete certainty. But seeing as there has been no presented reason to believe the generated surfaces are not convex, an optimization approach can be formulated.

### *4.3 Gradient Based Optimization in 4D*

#### *4.3.1 Search Background*

The visualization method presented in the last section provides a better understanding of the variations of PAE and ACPR through the dynamic search space. Multi-objective optimization techniques have been observed in previous works [56] where Steer used computer-aided algorithms in order to model and design large microwave circuits [16]. Genetic algorithms in the form of particle swarm have also been used previously to optimize microwave problems with multiple objectives [57, 58]. In order to be practical in real time communication systems, a search algorithm will have to quickly and automatically reconfigure through the use of one of these algorithms. Bandler even surveys different automatic optimization searches and how useful they are in microwave networks [59].

A type of power optimization algorithm has been presented by Li as a strategic method to help cognitive users communicate effectively by reducing interference incumbent to primary networks [60]. The use of a search algorithm to perform multidimensional momentum-aided circuit optimization has been shown to be beneficial for real-time cognitive radio reconfiguration [61]. This real-time reconfiguration has even been extended more recently into a higher-dimensional search space [62]. Chapter Three

has shown that search optimization is practical in three dimensions;  $Re(\Gamma_L)$ ,  $Im(\Gamma_L)$ , and  $P_{in}$  through a gradient-based search. It then follows that an increase in dimensionality can be optimized accordingly through a similar gradient search method.

To reconfigure in higher dimensions the gradient-based search will be implemented in a similar method to that used in Chapter Three. Equation 3.10 will be used as the main search vector where magnitudes  $D_a$  and  $D_b$  are calculated the same as in equation 3.3 and 3.4 respectively. Similarly to how input power  $P_{in}$  is normalized in equation 3.2, both gate-to-source voltage  $V_{GS}$  and drain-to-source voltage  $V_{DS}$  will be normalized. This ensures that both dimensions are given equal consideration in the evaluation of gradients. The user-defined maximum and the user-defined minimum  $V_{GS}$  and  $V_{DS}$  will be assigned a value of 1 and -1, respectively. The normalized  $v_{GS}$  and  $v_{DS}$  values are defined as follows:

$$v_{GS} = 2 \frac{V_{GS} - V_{GS,min}}{V_{GS,max} - V_{GS,min}} - 1 \quad (4.1)$$

$$v_{DS} = 2 \frac{V_{DS} - V_{DS,min}}{V_{DS,max} - V_{DS,min}} - 1 \quad (4.2)$$

In order to operate in higher dimensions, the search coordinate vector must be extended for both four and five dimensions. For a four-dimensional search algorithm, the  $V_{GS}$  neighboring gradient will be concatenated onto the ACPR and PAE unit coordinate vector calculations seen in equation 3.5 and equation 3.6. This change will result in the following for four-dimensional PAE and ACPR unit coordinate vectors;  $\hat{\Gamma}_r$ ,  $\hat{\Gamma}_i$ ,  $\hat{P}_{in}$ , and  $\hat{V}_{GS}$  by

$$\nabla p = \hat{\Gamma}_r \frac{\partial p}{\partial \Gamma_r} + \hat{\Gamma}_i \frac{\partial p}{\partial \Gamma_i} + \hat{P}_{in} \frac{\partial p}{\partial P_{in}} + \hat{V}_{GS} \frac{\partial p}{\partial v_{GS}} \quad (4.3)$$

$$\nabla a = \hat{\Gamma}_r \frac{\partial a}{\partial \Gamma_r} + \hat{\Gamma}_i \frac{\partial a}{\partial \Gamma_i} + \hat{p}_{in} \frac{\partial a}{\partial p_{in}} + \hat{v}_{GS} \frac{\partial a}{\partial v_{GS}} \quad (4.4)$$

The resulting five-dimensional PAE and ACPR unit coordinate vectors of  $\hat{\Gamma}_r, \hat{\Gamma}_i, \hat{P}_{in}, \hat{V}_{GS}$ , and  $\hat{V}_{DS}$  are

$$\nabla p = \hat{\Gamma}_r \frac{\partial p}{\partial \Gamma_r} + \hat{\Gamma}_i \frac{\partial p}{\partial \Gamma_i} + \hat{p}_{in} \frac{\partial p}{\partial p_{in}} + \hat{v}_{GS} \frac{\partial p}{\partial v_{GS}} + \hat{v}_{DS} \frac{\partial p}{\partial v_{DS}} \quad (4.5)$$

$$\nabla a = \hat{\Gamma}_r \frac{\partial a}{\partial \Gamma_r} + \hat{\Gamma}_i \frac{\partial a}{\partial \Gamma_i} + \hat{p}_{in} \frac{\partial a}{\partial p_{in}} + \hat{v}_{GS} \frac{\partial a}{\partial v_{GS}} + \hat{v}_{DS} \frac{\partial a}{\partial v_{DS}} \quad (4.6)$$

The measured change in PAE,  $\Delta p$ , as an extension of equation 3.7 will similarly be calculated as:

$$\frac{\partial p}{\partial v_{gs}} \approx \frac{\Delta p}{\Delta v_{gs}} = \frac{\Delta p}{D_n} \quad , \quad \frac{\partial p}{\partial v_{ds}} \approx \frac{\Delta p}{\Delta v_{ds}} = \frac{\Delta p}{D_n} \quad (4.7)$$

A similar process can be performed to find the change in ACPR,  $\Delta a$ . For the following four-dimensional and five-dimensional search algorithms, no predefined user ACPR constraint will be established. Unlike in Chapter Three, the ACPR limit will not be used in order to provide a proof of concept in a higher-dimensional search space. This is not to say that a constrained optimization in higher dimensions is not possible, as future directions of this work may aim to add a linearity constraint. Even without an ACPR limit, the gradient-based search utilizes ACPR gradient measurements in calculation of the bisector. Therefore, linearity remains a concern of the search rather than a requirement.

### 4.3.2 Four-Dimensional Simulation Results

The gradient-based search algorithm was first performed in simulation for the nonlinear Modelithics model of the Qorvo TGF2960 HEMT in four dimensions. The search is designed to maximize the PAE by optimizing the load-reflection coefficient  $\Gamma_L$ ,  $P_{in}$ , and  $V_{GS}$ . Simulation tests of the algorithm were performed using a step size  $D_s = 1$ , neighboring-point distance  $D_n = 0.05$ , an input power range  $-15 \text{ dBm} \leq P_{in} \leq 25 \text{ dBm}$ , and a gate-to-source voltage range  $-2 \text{ dBm} \leq V_{GS} \leq 2 \text{ dBm}$ , with  $V_{DS}$  held constant at  $5\text{V}$ . Figure 4.8 shows the search trajectory from the start location,  $\Gamma_L = 0.5\angle 0^\circ$ ,  $P_{in} = 5 \text{ dBm}$  and  $V_{GS} = -1\text{V}$ . Because this location was close to the optimum, only a total 18 measurement points were required to reach the final operation location of  $\Gamma_L = 0.45\angle 65.7^\circ$ ,  $P_{in} = 17.54 \text{ dBm}$  and  $V_{GS} = -1.59\text{V}$ . At this endpoint a power-added efficiency of 73.69% was obtained, which shows significant improvement when compared to the corresponding starting point efficiency of 17.96%. In order to depict the search's trajectory in four dimensions an additional Smith Tube is utilized. Together, both of these Smith Tubes share the x and y coordinates of  $Re(\Gamma_L)$  and  $Im(\Gamma_L)$  and differ in the z-dimension where one tube's z-coordinate represents input power  $P_{in}$  and the other's represents gate-to-source voltage  $V_{GS}$ .

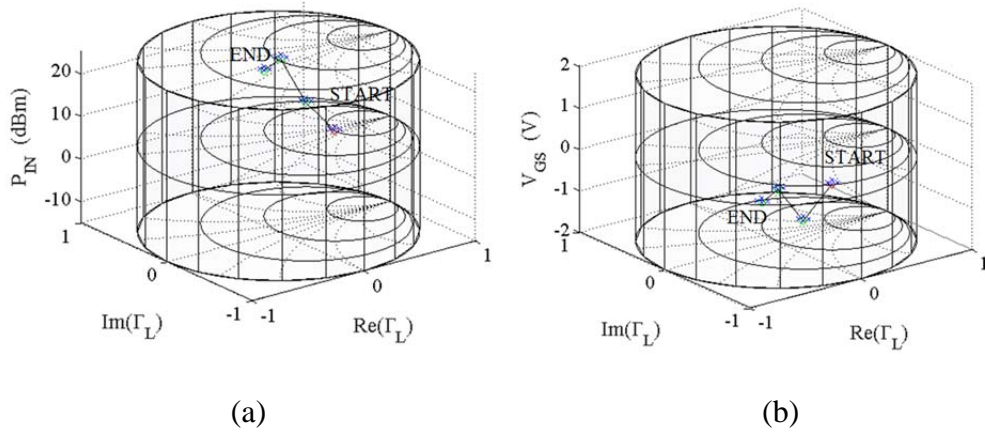


Figure 4.8: Search trajectory through the four dimensional space of  $\Gamma_r, \Gamma_i, P_{in}$ , and  $V_{GS}$  with parameters  $D_s = 1$ ,  $P_{in}$  range  $-15 \text{ dBm} \leq P_{in} \leq 25 \text{ dBm}$  and  $V_{GS}$  range  $-2\text{V} \leq V_{GS} \leq 2\text{V}$  and a starting location  $\Gamma_L = 0.5 \angle 0^\circ$ ,  $P_{in} = 5 \text{ dBm}$  and  $V_{GS} = -1\text{V}$ . The search required 18 measurement points and converged to the endpoint  $\Gamma_L = 0.45 \angle 65.7^\circ$ ,  $P_{in} = 17.54 \text{ dBm}$  and  $V_{GS} = -1.59 \text{ V}$ , where  $\text{PAE} = 73.69\%$ .

Figures 4.9 and 4.10 show the search results for additional starting combinations of  $\Gamma_L, P_{in}$ , and  $V_{GS}$ . Notice that while the starting locations are very different, the endpoint values of  $\Gamma_L, P_{in}$ , and  $\text{PAE}$  are very similar. This indicates that the searches converge to approximately the same location in the four-dimensional search space. Table 4.1 summarizes the search results for the different starting combinations in the four-dimensional search space. From the table, the end results indicate that the  $\text{PAE}$  varies less than 1%,  $P_{in}$  varies by 1 dBm, and  $V_{GS}$  varies by less than 0.2 V. However, the number of measurements required for each starting location varies greatly. This increase in measurements is expected as taking gradient calculations in higher dimensions requires exponentially more measurements and, as a result, starting locations further from the optimum require significantly more experimental queries.

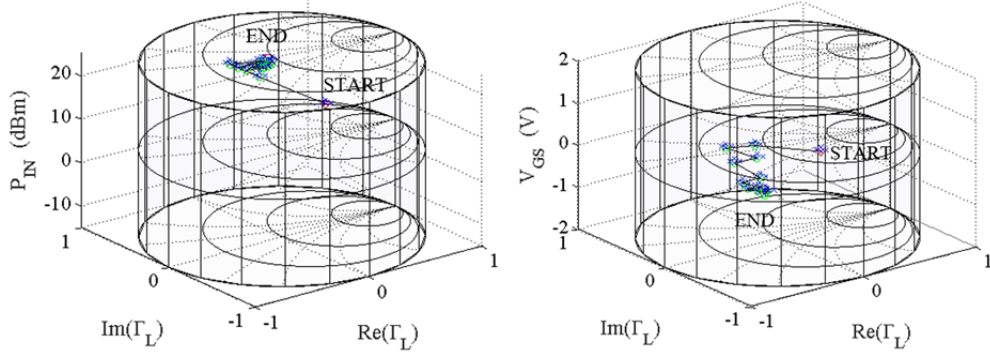


Figure 4.9: Search trajectory through the four dimensional space of  $\Gamma_r$ ,  $\Gamma_i$ ,  $P_{in}$ , and  $V_{GS}$  with parameters  $D_s = 1$ ,  $P_{in}$  range  $-15 \text{ dBm} \leq P_{in} \leq 25 \text{ dBm}$  and  $V_{GS}$  range  $-2V \leq V_{GS} \leq 2V$  and a starting location  $\Gamma_L = 0.5 \angle -90^\circ$ ,  $P_{in} = 20 \text{ dBm}$  and  $V_{GS} = 0V$ . The search required 86 measurement points and converged to the endpoint  $\Gamma_L = 0.45 \angle 60^\circ$ ,  $P_{in} = 18.90 \text{ dBm}$  and  $V_{GS} = -1.53V$ , where PAE = 74.65%.

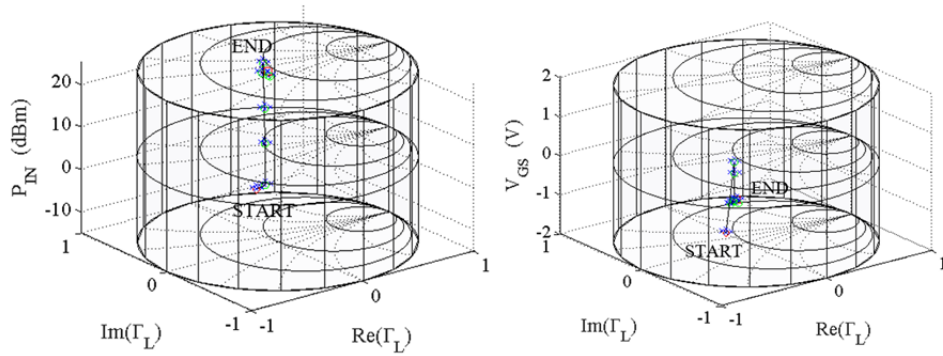


Figure 4.10: Search trajectory through the four dimensional space of  $\Gamma_r$ ,  $\Gamma_i$ ,  $P_{in}$ , and  $V_{GS}$  with parameters  $D_s = 1$ ,  $P_{in}$  range  $-15 \text{ dBm} \leq P_{in} \leq 25 \text{ dBm}$  and  $V_{GS}$  range  $-2V \leq V_{GS} \leq 2V$  and a starting location  $\Gamma_L = 0.25 \angle 90^\circ$ ,  $P_{in} = -5 \text{ dBm}$  and  $V_{GS} = -2V$ . The search required 45 measurement points and converged to the endpoint  $\Gamma_L = 0.48 \angle 61^\circ$ ,  $P_{in} = 19.46 \text{ dBm}$  and  $V_{GS} = -1.48V$ , where PAE = 74.74%.

TABLE 4.1: SUMMARY OF FOUR-DIMENSIONAL SIMUALATION RESULTS

Start $\Gamma_L$	Start $P_{in}$ (dBm)	Start $V_{GS}$ (V)	End $\Gamma_L$	End $P_{in}$ (dBm)	End $V_{GS}$ (V)	End PAE (%)	# Ms.
$0.5\angle 0^\circ$	5	-1	$0.45\angle 66^\circ$	17.54	-1.59	73.69	18
$0.25\angle 90^\circ$	-5	-2	$0.48\angle 61^\circ$	19.46	-1.48	74.74	45
$0\angle 0^\circ$	-15	-0.5	$0.49\angle 61^\circ$	19.27	-1.60	74.87	40
$0.75\angle 180^\circ$	10	1	$0.46\angle 62^\circ$	19.55	-1.51	74.74	92
$0.5\angle -90^\circ$	20	0	$0.45\angle 60^\circ$	18.90	-1.53	74.65	86

#### 4.3.3 Five-Dimensional Simulation Results

For the same nonlinear Modelithics Qorvo TGF2960 HEMT model a fifth real parameter,  $V_{DS}$ , was included in the search. The search contains the same optimization goal as in the previous section, which is to maximize the PAE by optimizing the load-reflection coefficients  $\Gamma_L$ ,  $P_{in}$ ,  $V_{GS}$  and  $V_{DS}$  simultaneously. Searches done in simulation were performed using a step size  $D_s = 1$ , neighboring-point distance  $D_n = 0.05$ , an input power range  $-15 \text{ dBm} \leq P_{in} \leq 25 \text{ dBm}$ , a gate to source voltage range  $-2 \text{ dBm} \leq V_{GS} \leq 2 \text{ dBm}$ , and a  $V_{DS}$  range  $2 \text{ dBm} \leq V_{DS} \leq 12 \text{ dBm}$ . In order to display the trajectory of the search in five dimensions, a third Smith Tube will be provided. Similarly to Section 4.2.2, the extra Smith Tube will share x and y coordinates of  $Re(\Gamma_L)$  and  $Im(\Gamma_L)$  but will differ in the z-dimension. The z-dimension for the following three tubes used to depict the trajectory of the search will be  $P_{in}$ ,  $V_{GS}$ , and  $V_{DS}$ . Figure 4.11 provides an example of the search trajectory through the five-dimensional search space with three total tubes from the starting location  $\Gamma_L = 0.75\angle 180^\circ$ ,  $P_{in} = 10 \text{ dBm}$ ,  $V_{GS} = 1 \text{ V}$ , and  $V_{DS} = 9 \text{ V}$ . The search took a total of 44 measurement points before converging to an optimum

location of  $\Gamma_L = 0.43\angle 62^\circ$   $P_{in}=20.17$  dBm,  $V_{GS} = -1.44V$ , and  $V_{DS} = 5.04V$ . At the final operating point a PAE = 75.05% was achieved.

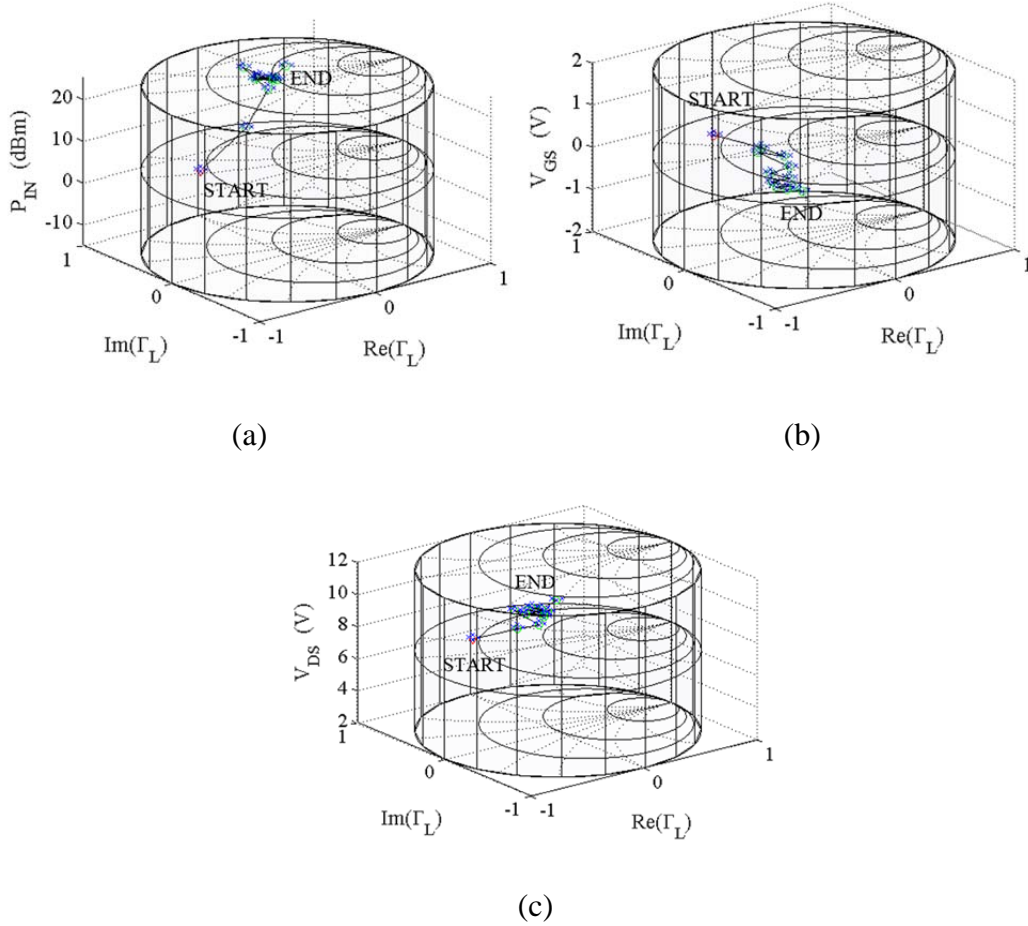


Figure 4.11: Search trajectory through the five dimensional space of  $\Gamma_r$ ,  $\Gamma_i$ ,  $P_{in}$ ,  $V_{GS}$ , and  $V_{DS}$  with parameters  $D_s = 1$ ,  $P_{in}$  range  $-15$  dBm  $\leq P_{in} \leq 25$  dBm,  $V_{GS}$  range  $-2V \leq V_{GS} \leq 2V$ ,  $V_{DS}$  range  $2V \leq V_{DS} \leq 12V$  and a starting location  $\Gamma_L = 0.75\angle 180^\circ$ ,  $P_{in} = 10$  dBm,  $V_{GS} = 1V$  and  $V_{DS} = 9V$ . The search required 82 measurement points and converged to the endpoint  $\Gamma_L = 0.55\angle 54^\circ$   $P_{in}=23.30$  dBm,  $V_{GS} = -1.49V$ , and  $V_{DS} = 8.50V$ , where PAE = 75.52%.

Figure 4.12 shows the search results for a different starting combination of  $\Gamma_L$ ,  $P_{in}$ ,  $V_{GS}$ , and  $V_{DS}$ . The results for multiple starting location combinations can be seen in Table 4.2. The results show that the final values of PAE vary by less than 2%. This is

particularly impressive because the starting PAE for each search was no greater than 32.48% and the average starting PAE for all five searches was 10.10%. The consistency in ending PAE for each search illustrates the robustness of the search from across the five-dimensional optimization space. Even without initial information the search is able to adjust operating characteristics accordingly to find an optimum location that provides high efficiency.

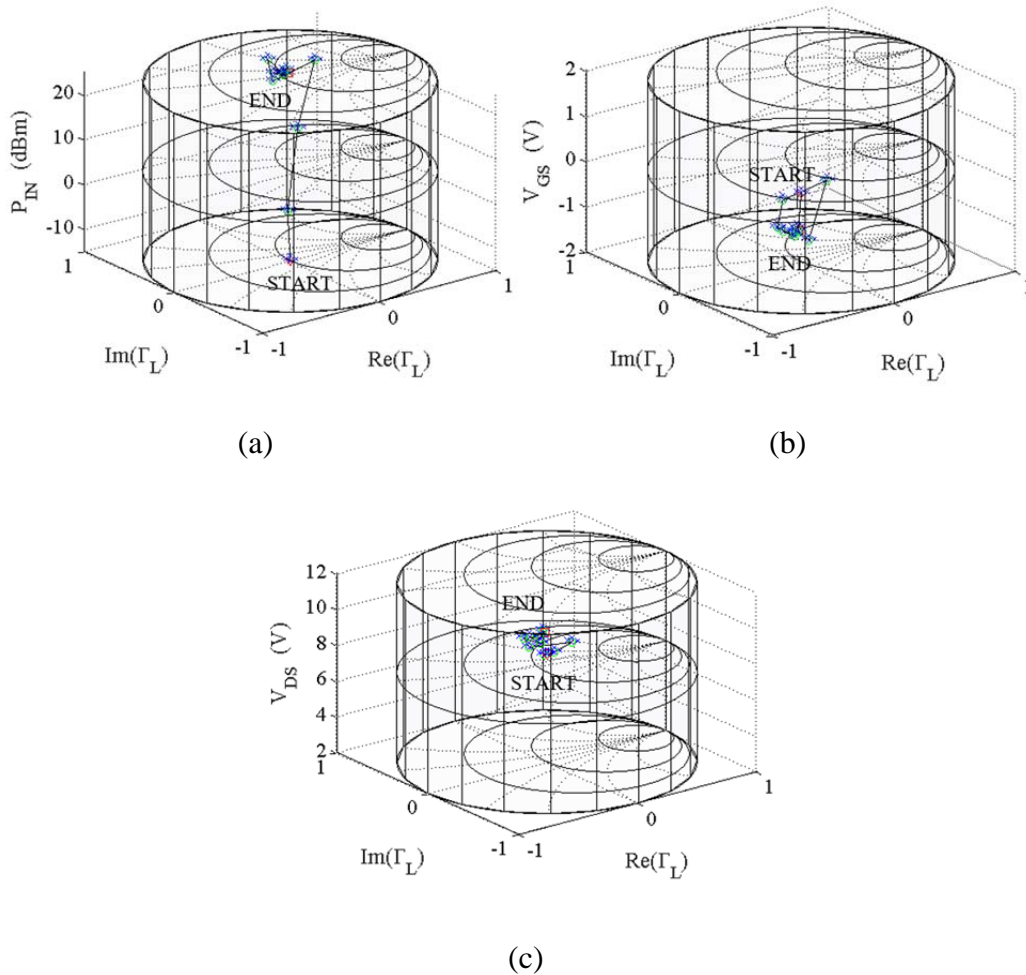


Figure 4.12: Search trajectory through the five dimensional space of  $\Gamma_r$ ,  $\Gamma_i$ ,  $P_{in}$ ,  $V_{GS}$ , and  $V_{DS}$  with parameters  $D_s = 1$ ,  $P_{in}$  range  $-15 \text{ dBm} \leq P_{in} \leq 25 \text{ dBm}$ ,  $V_{GS}$  range  $-2V \leq V_{GS} \leq 2V$ ,  $V_{DS}$  range  $2V \leq V_{DS} \leq 12V$  and a starting location  $\Gamma_L = 0 \angle 0^\circ$ ,  $P_{in} = -15 \text{ dBm}$ ,  $V_{GS} = -0.5V$  and  $V_{DS} = 8V$ . The search required 75 measurement points and converged to the endpoint  $\Gamma_L = 0.53 \angle 54^\circ$ ,  $P_{in} = 20.77 \text{ dBm}$ ,  $V_{GS} = -1.93V$ , and  $V_{DS} = 7.70V$ , where  $\text{PAE} = 76.53\%$ .

TABLE 4.2: SUMMARY OF FIVE-DIMENSIONAL SIMULATION RESULTS

Start $\Gamma_L$	Start $P_{in}$ (dBm)	Start $V_{GS}$ (V)	Start $V_{DS}$ (V)	End $\Gamma_L$	End $P_{in}$ (dBm)	End $V_{GS}$ (V)	End $V_{DS}$ (V)	End PAE (%)	# Ms.
$0.5\angle 0^\circ$	5	-1	6	$0.54\angle 54^\circ$	19.65	-1.84	5.98	75.80	74
$0.25\angle 90^\circ$	-5	-2	5	$0.43\angle 62^\circ$	19.43	-1.49	4.79	74.41	51
$0\angle 0^\circ$	-15	-0.5	8	$0.53\angle 54^\circ$	20.77	-1.93	7.70	76.53	75
$0.75\angle 180^\circ$	10	1	9	$0.55\angle 54^\circ$	23.30	-1.49	8.50	75.52	82
$0.5\angle -90^\circ$	20	0	3	$0.49\angle 60^\circ$	20.17	-1.52	5.50	75.10	105

#### 4.4 Summary

This chapter presents a new method of visualization within both a four and five-dimensional search space, providing a foundation for development of multi-dimensional circuit optimization algorithms for real-time application as well as for nonlinear power amplifier simulation- and measurement-based design. Through the use of a grid of Power Smith Tubes, the tradeoff of power amplifier linearity and efficiency can be seen simultaneously. As a result, the four and five-dimensional optimization problem can be more thoroughly identified and therefore optimized accordingly. Simulation results have demonstrated this tool's promise for application in real-time power amplifier reconfiguration and general power amplifier design. By allowing visualization, a solution to quickly optimize in higher dimensions can be developed accordingly.

A gradient-based search has been proposed and tested in both four and five dimensions. In four dimensions this unconstrained search is able to reach a consistent optimum operating location. The gradient search has also been shown to perform consistently with the increase in input parameters to a total of five dimensions. The search results in both four and five dimensions have indicated that the search can

effectively reconfigure power amplifier operating characteristics in order to achieve a more desirable PAE. With the gradient search proven to be viable in up to five dimensions there is no reason to believe the dimensionality of the search could not be increased to include more input optimization parameters.

## CHAPTER FIVE

### Conclusions

A novel method of visualization and optimization has been presented which shows promise in facilitating fast reconfiguration of power amplifiers. With the use of this search algorithm, cognitive and adaptive radar transmitters are expected to optimize for higher linearity and efficiency through the simultaneous adjustment of operating characteristics. The Power Smith Tube has been presented as a method to visualize the tradeoff between efficiency and linearity. Simultaneous optimization of both the load reflection coefficient and input power has been demonstrated in a reasonably small amount of experimental queries. Visualization of higher-dimensional searches has been shown, and initial unconstrained multi-parameter circuit optimizations using this space have been demonstrated.

The continuation of this work addresses the extension of the constrained optimization to multiple variables. Extending the constrained gradient-based optimization to additional dimensions is not expected to be without some challenge. The success of the gradient algorithm is, in large part, dependent upon the assumption of Zadeh convexity [43]. Zadeh convexity has been shown to occur in several experiments where the search is able to successfully optimize accordingly. However, when the dimensionality of the search is increased past three, the search space becomes increasingly difficult to fully conceptualize. Attempts can be made to illustrate the convexity in higher dimensions, but without the ability to fully characterize higher dimensions, convexity cannot be assumed

with absolute certainty. Without convexity any search algorithm performed runs the risk of converging to a local minimum instead of the desired global minimum. Aside from possessing absolute convexity, the main goal of the search algorithm is to quickly reconfigure a power amplifier in order to achieve more favorable operating characteristics. The proposed gradient-based search has been shown to accomplish this goal by increasing power amplifier performance when compared to initial operating locations. In many cases where convexity does not exist, knowledge about the device's behavior, even the linear S-parameters, is expected to assist at some level in obtaining useful results from the optimization.

Future contributions of this work can be expected to extend the optimization to a greater number of input parameters, which would allow for full autonomous circuit reconfiguration. Along with the increase in input parameters, more design goals or objectives may be imposed on the search to increase the subsequent search's effectiveness. This work makes a significant contribution toward the progression of joint circuit and waveform optimization through the autonomous reconfiguration of circuit parameters. This reconfigurability will prove useful to both cognitive radar and wireless communication systems by allowing each to adjust current operating parameters based upon their surrounding spectral environments. In addition, the algorithms mentioned in this thesis should be adjusted for operation in a tunable amplifier and tested on the tunable amplifier platform.

## BIBLIOGRAPHY

- [1] R. Hajji, F. Beaugerard, and F.M. Ghannouchi, "Multitone Power and Intermodulation Load-Pull Characterization of Microwave Transistors Suitable for Linear SSPA's Design," *IEEE Transactions on Microwave Theory and Techniques*, Vol. 45, No. 7, July 1997, pp. 1093-1099.
- [2] D.M. Snider, "A Theoretical Analysis and Experimental Confirmation of the Optimally Loaded and Overdriven RF Power Amplifier," *IEEE Transactions on Electron Devices*, Vol. ED-14, No. 12, December 1967, pp. 851-857.
- [3] J.-S. Fu and A. Mortazawi, "Improving Power Amplifier Efficiency and Linearity Using a Dynamically Controlled Tunable Matching Network," *IEEE Transactions on Microwave Theory and Techniques*, Vol. 56, No. 12, December 2008, pp. 3239-3244.
- [4] Sevic, J.F.; Burger, K.L.; Steer, M.B., "A novel envelope-termination load-pull method for ACPR optimization of RF/microwave power amplifiers," in *Microwave Symposium Digest, 1998 IEEE MTT-S International*, vol.2, no., pp.723-726 vol.2, 7-12 June 1998
- [5] Guarnieri, M., "The Age of Vacuum Tubes: Early Devices and the Rise of Radio Communications [Historical]," in *Industrial Electronics Magazine, IEEE*, vol.6, no.1, pp.41-43, March 2012
- [6] Brennan, L.E. and Reed, I.S.; "Theory of Adaptive Radar," *IEEE Transactions on Aerospace and Electronic Systems*, Vol. AES-9, No. 2, March 1973, pp. 237-252.
- [7] Haimovich, A., "The eigencanceler: adaptive radar by eigenanalysis methods," in *Aerospace and Electronic Systems, IEEE Transactions on*, vol.32, no.2, pp.532-542, April 1996
- [8] Melvin, W.L., "Space-time adaptive radar performance in heterogeneous clutter," in *Aerospace and Electronic Systems, IEEE Transactions on*, vol.36, no.2, pp.621-633, Apr 2000

- [9] Guerci, J.R., "Cognitive radar: A knowledge-aided fully adaptive approach," in Radar Conference, 2010 IEEE , vol., no., pp.1365-1370, 10-14 May 2010
- [10] Melvin, W.L.; Wicks, M.C., "Improving practical space-time adaptive radar," in Radar Conference, 1997., IEEE National , vol., no., pp.48-53, 13-15 May 1997
- [11] M.D. Weiss, F.H. Raab, and Z. Popovic, "Linearity of X-Band Class-F Power Amplifiers in High-Efficiency Transmitters," IEEE Transactions on Microwave Theory and Techniques, Vol. 49, No. 6, June 2001, pp. 1174-1179.
- [12] Y. Lu, D. Peroulis, S. Mohammadi, and L. Katehi, "A MEMS Reconfigurable Matching Network," IEEE Microwave and Wireless Components Letters, Vol. 13, No. 10, October 2003, pp. 437-439.
- [13] Vaka-Heikkila, T. and Rebeiz, G; "A 4 – 18 GHz Reconfigurable RF MEMS Matching Network for Power Amplifier Applications," International Journal of RF and Microwave Computer-Aided Engineering, Vol. 14, No. 4, pp. 356-372, July 2004.
- [14] Sievenpiper, Dan; Schaffner, J.; Loo, R.; Tangonan, G.; Ontiveros, S.; Harold, R., "A tunable impedance surface performing as a reconfigurable beam steering reflector," in Antennas and Propagation, IEEE Transactions on , vol.50, no.3, pp.384-390, Mar 2002
- [15] Nemati, H.M.; Fager, C.; Gustavson, U.; Jos, R.; and Zirath, H.; "Design of Varactor-Based Tunable Matching Networks for Dynamic Load Modulation of High Power Amplifiers," IEEE Transactions on Microwave Theory and Techniques, Vol. 57, No. 5, May 2009, pp. 1110-1118.
- [16] M.B. Steer, J.W. Bandler, and C.M. Snowden, "Computer-Aided Design of RF and Microwave Circuits and Systems," IEEE Transactions on Microwave Theory and Techniques, Vol. 50, No. 3, March 2002, pp. 996-1005.
- [17] F. Li, L. Wang, J. Hua, L. Meng, and J. Zhang, "Power optimization for dynamic spectrum access with convex optimization and intelligent algorithm," Wireless Networks (2015) 21: 161-172.
- [18] Qiao, D; Molfino, R; Lardizabal, S.; Pillans, B.; Asbeck, P. and Jerinic, G.; "An Intelligently Controlled RF Power Amplifier with a Reconfigurable MEMS-Varactor Tuner," IEEE Transactions on Microwave Theory and Techniques, Vol. 53, No. 3, Part 2, March 2005, pp. 1089-1095.

- [19] du Plessis, W. and Abrie, P.; "Lumped Impedance Matching Using a Hybrid Genetic Algorithm," *Microwave and Optical Technology Letters*, Vol. 37, No. 3, pp. 210-212, May 2003.
- [20] J. Barkate, M. Flachsbar, Z. Hays, M. Fellows, J. Barlow, C. Baylis, L. Cohen, and R.J. Marks II, "Fast, Simultaneous Optimization of Power Amplifier Input Power and Load Impedance for Power-Added Efficiency and Adjacent-Channel Power Ratio Using the Power Smith Tube," accepted for publication in *IEEE Transactions on Aerospace and Electronic Systems*, October 2015.
- [21] Martin, J.; Baylis, C.; Cohen, L.; de Graaf, J.; and Marks II, R.J.; "A Peak-Search Algorithm for Load-Pull Optimization of Power-Added Efficiency and Adjacent-Channel Power Ratio," *IEEE Transactions on Microwave Theory and Techniques*, Vol. 62, No. 8, August 2014, pp. 1772-1783.
- [22] Miettinen, K.; *Nonlinear Multiobjective Optimization*, Kluwer Academic Publishers, 1998.
- [23] Y. Collette and P. Siarry, *Multiobjective Optimization: Principles and Case Studies*, Springer, 2004.
- [24] R.T. Marler and J.S. Arora. "Survey of Multi-Objective Optimization Methods for Engineering." *Structural and Multidisciplinary Optimization* 26.6 (2004): 369-395.395.
- [25] H.C. Calpine and A. Golding, "Some Properties of Pareto-Optimal Choices in Decision Problems," *Omega* 4, No. 2 (1976): 141-147.
- [26] T. Getachew, M. Kostreva, and L. Lancaster. "A Generalization of Dynamic Programming for Pareto Optimization in Dynamic Networks." *RAIRO-Operations Research* 34.1 (2000): 27-47.
- [27] M. Fellows, M. Flachsbar, J. Barlow, C. Baylis, L. Cohen, and R.J. Marks II, "The Smith Tube: Selection of Radar Chirp Waveform Bandwidth and Power Amplifier Load Impedance Using Multiple-Bandwidth Load-Pull Measurements," 2014 *IEEE Wireless and Microwave Technology Conference (WAMICON 2014)*, Tampa, Florida, June 2014.
- [28] C. Zelle, "A Spherical Representation of the Smith Chart," *IEEE Microwave Magazine*, Vol. 8, Issue 3, June 2007, pp. 60-66.

- [29] Y. Wu, Y. Zhang, Y. Liu, and H. Huang, "Theory of the Spherical Generalized Smith Chart," *Microwave and Optical Technology Letters*, Vol. 51, Issue 1, November 2008, pp. 95-97.
- [30] A. Shamin, A.G. Radwan, and K.N. Salama, "Fractional Smith Chart Theory," *IEEE Microwave and Wireless Components Letters*, Vol. 21, No. 3, March 2011, pp. 117-119.
- [31] J. Kretzschmar and D. Schoonaert, "Smith Charts for Lossy Transmission Lines," *Proceedings of the IEEE*, Vol. 57, No. 9, September 1969, pp. 1658-1660.
- [32] M. Ubostad and M. Olavsbraten, "Linearity performance of an RF Power Amplifier under Different Bias and Load Conditions With and Without DPD," 2010 IEEE Radio and Wireless Symposium Digest, pp. 232-235.
- [33] J. Barkate, M. Fellows, J. Barlow, C. Baylis, L. Cohen, and R.J. Marks II, "The Power Smith Tube: Joint Optimization of Power Amplifier Input Power and Load Impedance for Power-Added Efficiency and Adjacent-Channel Power Ratio," Submitted February 2015 to the 2015 IEEE Wireless and Microwave Technology Conference, Cocoa Beach, Florida, April 2015.
- [34] Okada, K.; Yoshihara, Y.; Sugawara, H.; Masu, K., "A dynamic reconfigurable RF circuit architecture," in Design Automation Conference, 2005. Proceedings of the ASP-DAC 2005. Asia and South Pacific , vol.2, no., pp.683-686 Vol. 2, 18-21 Jan. 2005
- [35] N. Deve, A. Kouki, and V. Nerguizian, "A Compact Size Reconfigurable 1 – 3 GHz Impedance Tuner Suitable for RF MEMS Applications," Proceedings of the 16th International Conference on Microelectronics, 2004 (ICM 2004), December 6-8, 2004, pp. 101-104.
- [36] Y. Sun, J. Moritz, and X. Zhu, "Adaptive Impedance Matching and Antenna Tuning for Green Software-Defined and Cognitive Radio," 54th IEEE International Midwest Symposium on Circuits and Systems, 2011, pp. 1-4.
- [37] Dongjiang Qiao; Molfino, R.; Lardizabal, S.M.; Pillans, Brandon; Asbeck, P.M.; Jerinic, G., "An intelligently controlled RF power amplifier with a reconfigurable MEMS-varactor tuner," in Microwave Theory and Techniques, IEEE Transactions on , vol.53, no.3, pp.1089-1095, March 2005

- [38] C. Baylis, M. Fellows, L. Cohen, and R.J. Marks II, "Solving the Spectrum Crisis: Intelligent, Reconfigurable Microwave Transmitter Amplifiers for Cognitive Radar," *IEEE Microwave Magazine*, Vol. 15, No. 5, July 2014, pp. 94-107.
- [39] S.D. Blunt, M. Cook, J. Jakabosky, J. de Graaf, and E. Perrins, "Polyphase-coded FM (PCFM) Radar Waveforms, Part 1: Implementation," *IEEE Transactions on Aerospace and Electronic Systems*, Vol. 50, No. 3, pp. 2218-2229, July 2014.
- [40] S.D. Blunt, J. Jakabosky, M. Cook, J. Stiles, S. Seguin, and E.L. Mokole, "Polyphase-Coded (PCFM) Radar Waveforms, Part II: Optimization," *IEEE Transactions on Aerospace and Electronic Systems*, Vol. 50, No. 3, July 2014, pp. 2230-2241.
- [41] C. Baylis, L. Wang, M. Moldovan, J. Martin, H. Miller, L. Cohen, and J. de Graaf, "Designing Transmitters for Spectral Conformity: Power Amplifier Design Issues and Strategies," *IET Radar, Sonar & Navigation*, Vol. 5, No. 6, July 2011, pp. 681-685.
- [42] M. Fellows, C. Baylis, J. Martin, L. Cohen, and R.J. Marks II, "Direct Algorithm for the Pareto Load-Pull Optimization of Power-Added Efficiency and Adjacent-Channel Power Ratio," *IET Radar, Sonar & Navigation*, Vol. 8, No. 9, December 2014, pp. 1280-1287.
- [43] L. Zadeh, "Fuzzy Sets," *Information Control*, Vol. 5, pp. 338-353, 1965. Reprinted in J.C. Bezdek and S.K. Pal, *Fuzzy Models for Pattern Recognition*, IEEE Press, 1992.
- [44] Leaves, P.; Moessner, K.; Tafazolli, R.; Grandblaise, D.; Bourse, D.; Tönjes, R.; Breveglieri, M., "Dynamic spectrum allocation in composite reconfigurable wireless networks," in *Communications Magazine, IEEE*, vol.42, no.5, pp.72-81, May 2004
- [45] A.M.M. Mohamed, S. Boumaiza, and R.R. Mansour, "Novel Reconfigurable Fundamental/Harmonic Matching Network for Enhancing the Efficiency of Power Amplifiers," 2010 European Microwave Conference, Paris, France, September 2010, pp. 1122-1125.
- [46] G. Qiu, M.R. Varley, and T.J. Terrell, "Accelerated Training of Backpropagation Networks by Using Adaptive Momentum Step," *IEE Electronics Letters*, Vol. 28, No. 4, February 1992, pp. 377-379.

- [47] P. Arabshahi, J.J.Choi, R.J.Marks II and T.P. Caudell "Fuzzy Control of Backpropagation," Proc. First IEEE International Conference on Fuzzy Systems, (FUZZ-IEEE 1992) San Diego, pp. 967-972, March 1992.
- [48] R.D.Reed and R.J.Marks II, Neural Smithing, MIT Press, 1999.
- [49] Jeonghyeon Cha; Youngoo Yang; Bumjae Shin; Bumman Kim, "An adaptive bias controlled power amplifier with a load-modulated combining scheme for high efficiency and linearity," in Microwave Symposium Digest, 2003 IEEE MTT-S International , vol.1, no., pp.81-84 vol.1, 8-13 June 2003
- [50] F.H. Raab, "High-Efficiency Linear Amplification by Dynamic Load Modulation," 2003 IEEE MTT-S International Microwave Symposium Digest, Philadelphia, Pennsylvania, June 2003, Vol. 3, pp. 1717-1720.
- [51] Y. Yang, K. Choi, and K.P. Weller, "DC Boosting Effect of Active Bias Circuits and Its Optimization for Class-AB InGaP-GaAs HBT Power Amplifiers," IEEE Transactions on Microwave Theory and Techniques, Vol. 52, No. 5, pp.1455-1463.
- [52] X. Blasco, J.M. Herrero, J. Sanchis, M. Martinez. " A new graphical visualization of n-dimensional Pareto front for decision-making in multiobjective optimization" Information Sciences, October 2008, Vol. 178, Is. 20, pp. 3908-3924
- [53] E. Kandogan " Visualizing Multi-dimensional Clusters, Trends, and Outliers using Star Coordinates" Proceedings of the seventh ACM SIGKDD international conference on knowledge discovery and data mining, pp. 107-116 (2001)
- [54] Feiner, Steven K., and Clifford Beshers. "Worlds within Worlds: Metaphors for Exploring n-Dimensional Virtual Worlds." Proceedings of the 3rd Annual ACM SIGGRAPH Symposium on User Interface Software and Technology. ACM, 1990.
- [55] Fisher,R.A. "The use of multiple measurements in taxonomic problems" Annual Eugenics, 7, Part II, 179-188 (1936)
- [56] C. Charalambous, "A Unified Review of Optimization," IEEE Transactions on Microwave Theory and Techniques, Vol. 22, No. 3, March 1974, pp. 289-300.
- [57] S. K. Goudos, J. N. Sahalos "Microwave Absorber Optimal Design Using Multi-Objective Particle Swarm Optimization" Microwave and Optical Technology Letters, August, 2006. 10.1002

- [58] Goudos, S.K.; Zaharis, Z.D.; Kampitaki, D.G.; Rekanos, I.T.; Hilaris, C.S., "Pareto Optimal Design of Dual-Band Base Station Antenna Arrays Using Multi-Objective Particle Swarm Optimization With Fitness Sharing," in *Magnetics, IEEE Transactions on* , vol.45, no.3, pp.1522-1525, March 2009
- [59] J.W. Bandler, "Optimization Methods for Computer-Aided Design," IEEE Transactions on Microwave Theory and Techniques, Vol. 17, No. 8, August 1969, pp. 533-552.
- [60] F. Li, L. Wang, J. Hua, L. Meng, and J. Zhang, "Power optimization for dynamic spectrum access with convex optimization and intelligent algorithm," *Wireless Networks* (2015) 21: 161-172.
- [61] J. Barkate, A. Tstatsoulas, M. Fellows, M. Flachsbart, C. Baylis, L. Cohen, R.J. Marks II, "Fast, Momentum-Aided Optimization of Transmitter Amplifier Load Impedance and Input Power for Cognitive Radio Using the Power Smith Tube" *2016 IEEE Radio and Wireless Symposium (RWS)*, Austin, TX, USA, 2016, pp. 54-56.
- [62] J. Barkate, A. Tstatsoulas, C. Baylis, L. Cohen, R.J. Marks II, "Comparison of Multidimensional Circuit Optimization Techniques for Real-Time Transmitter Use" *Wireless and Microwave Circuits and Systems (WMCS), 2016 Texas Symposium on*, Waco, TX, 2016